THE REST-FRAME H-BAND LUMINOSITY FUNCTION OF RED SEQUENCE GALAXIES IN CLUSTERS AT $1.0 < Z < 1.3$

Jeffrey C.C. Chan[1], Gillian Wilson[1], Gregory Rudnick[2], Adam Muzzin[3], Michael Balogh[4], Julie Nantais[5],
Remco F. J. van der Burg[6], Pierluigi Cerulo[7], Andrea Biviano[8], Michael C. Cooper[9], Ricardo Demarco[7], Ben Forrest[1],
Chris Lidman[10], Allison Noble[11], Lyndsay Old[12], Irene Pintos-Castro[12], Andrew M. M. Reeves[4], Kristi A. Webb[4],
Howard K.C. Yee[12], Mohamed H. Abdullah[1,13], Gabriella De Lucia[8], Danilo Marchesini[14], Sean L. McGee[15],
Mauro Stefanon[16] and Dennis Zaritsky[17]

[1]Department of Physics & Astronomy, University of California, Riverside, 900 University Avenue, Riverside, CA 92521, USA
[2]Department of Physics and Astronomy, The University of Kansas, Malott room 1082, 1251 Wescoe Hall Drive, Lawrence, KS 66045, USA
[3]Department of Physics and Astronomy, York University, 4700 Keele Street, Toronto, Ontario, ON MJ3 1P3, Canada
[4]Department of Physics and Astronomy, University of Waterloo, Waterloo, Ontario, N2L 3G1, Canada
[5]Departamento de Ciencias Físicas, Universidad Andres Bello, Fernandez Concha 700, Las Condes 7591538, Santiago, Región Metropolitana, Chile
[6]European Southern Observatory, Karl-Schwarzschild-Str. 2, 85748, Garching, Germany
[7]Departamento de Astronomía, Facultad de Ciencias Físicas y Matemáticas, Universidad de Concepción, Concepción, Chile
[8]INAF-Osservatorio Astronomico di Trieste, via G. B. Tiepolo 11, 34143, Trieste, Italy
[9]Department of Physics and Astronomy, University of California, Irvine, 4129 Frederick Reines Hall, Irvine, CA 92697, USA
[10]The Research School of Astronomy and Astrophysics, Australian National University, ACT 2601, Australia
[11]MIT Kavli Institute for Astrophysics and Space Research, 70 Vassar St, Cambridge, MA 02109, USA
[12]Department of Astronomy and Astrophysics, University of Toronto 50 St. George Street, Toronto, Ontario, M5S 3H4, Canada
[13]Department of Astronomy, National Research Institute of Astronomy and Geophysics, 11421 Helwan, Egypt
[14]Physics and Astronomy Department, Tufts University, Robinson Hall, Room 257, Medford, MA 02155, USA
[15]School of Physics and Astronomy, University of Birmingham, Edgbaston, Birmingham B15 2TT, England
[16]Leiden Observatory, Leiden University, NL-2300 RA Leiden, Netherlands
[17]Steward Observatory and Department of Astronomy, University of Arizona, Tucson, AZ, 85719

Draft version June 27, 2019

ABSTRACT

We present results on the rest-frame H-band luminosity functions (LF) of red sequence galaxies in seven clusters at $1.0 < z < 1.3$ from the Gemini Observations of Galaxies in Rich Early Environments Survey (GOGREEN). Using deep GMOS-z' and IRAC 3.6μm imaging, we identify red sequence galaxies and measure their LFs down to $M_H \sim M_H^* + (2.0 - 3.0)$. By stacking the entire sample, we derive a shallow faint end slope of $\alpha \sim -0.35^{+0.15}_{-0.15}$ and $M_H^* \sim -23.52^{+0.15}_{-0.17}$, suggesting that there is a deficit of faint red sequence galaxies in clusters at high redshift. By comparing the stacked red sequence LF of our sample with a sample of clusters at $z \sim 0.6$, we find an evolution in the faint end of the red sequence over the ~ 2.6 Gyr between the two samples, with the mean faint end red sequence luminosity growing by more than a factor of two. The faint-to-luminous ratio of our sample ($0.78^{+0.19}_{-0.15}$) is consistent with the trend of decreasing ratio with increasing redshift as proposed in previous studies. A comparison with the field shows that the faint-to-luminous ratios in clusters are consistent with the field at $z \sim 1.15$ and exhibit a stronger redshift dependence. Our results support the picture that the build up of the faint red sequence galaxies occurs gradually over time and suggest that faint cluster galaxies, similar to bright cluster galaxies, experience the quenching effect induced by environment already at $z \sim 1.15$.

Subject headings: galaxies: clusters: general – galaxies: elliptical and lenticular, cD – galaxies: luminosity function, mass function – galaxy: evolution – galaxies: high-redshift

1. INTRODUCTION

In the local universe, the galaxy population in the high density environment comprises mainly red, passive galaxies, as reflected by their higher quiescent fraction at fixed stellar mass than in the field (e.g. Sandage & Visvanathan 1978; Balogh et al. 2004; Baldry et al. 2006; Wetzel et al. 2012). The red galaxies in the highest-density environment, i.e. galaxy clusters, have mostly early-type morphology and are mainly composed of old stellar populations (e.g. Dressler 1980; Kodama & Arimoto 1997; Thomas et al. 2005; Trager et al. 2008; Thomas et al. 2010). They reside in a well-defined region of the color-magnitude space, known as the red sequence (e.g. Bower et al. 1992, 1998; Kodama et al. 1998). Understanding how these red sequence galaxies form and evolve and the

physical processes involved remains as one of the major goals in extragalactic astronomy.

Over the last decade, much effort has been made in determining the evolution of the red sequence galaxy population in clusters out to intermediate and high redshift. One widely used method to trace their evolution is the cluster galaxy luminosity function (LF), which measures the number of galaxies per luminosity interval. This direct and powerful statistical tool encodes information about the star formation and mass assembly history of the galaxies, hence it can provide strong constraints for models of galaxy formation and evolution. For example, previous studies have shown that the evolution of bright galaxies in clusters is consistent with passive evolution through studying the bright end of the red sequence cluster LF or the total cluster LF out to $z \sim 1.5$ (e.g. Ellis et al. 1997; De Propris et al. 1999, 2007, 2013; Lin et al. 2006; Andreon 2008;

Muzzin et al. 2007, 2008; Rudnick et al. 2009; Strazzullo et al. 2010; Mancone et al. 2012).

The extent of the evolution of the faint red sequence population, however, is still under debate. As opposed to local clusters that exhibit a flat faint end, or even an upturn at the faint end of their red sequence LFs (e.g. Popesso et al. 2006; Agulli et al. 2014; Moretti et al. 2015; Lan et al. 2016), various studies have revealed that clusters at intermediate and high redshifts show a continual decrease in fraction of the faint red sequence population with redshift, which indicates a gradual build up of the faint red sequence population over time since $z \sim 1.5$ (e.g. Dressler et al. 1997; Smail et al. 1998; Kodama et al. 2004; De Lucia et al. 2004, 2007; Tanaka et al. 2007; Gilbank et al. 2008; Rudnick et al. 2009; Stott et al. 2009; Rudnick et al. 2012; Martinet et al. 2015; Zenteno et al. 2016; Zhang et al. 2017; Sarron et al. 2018). This is also supported by findings that cluster galaxies on the high mass end of the red sequence are on average older than the low mass end (e.g. Nelan et al. 2005; Sánchez-Blázquez et al. 2009; Demarco et al. 2010b; Smith et al. 2012). Contrary to the abovementioned studies, a number of studies have reported that there is little or no evolution in the faint end of red sequence cluster LF up to $z \sim 1.5$ (e.g. Andreon 2006; Crawford et al. 2009; De Propris et al. 2013, 2015; Andreon et al. 2014; Cerulo et al. 2016), which in turn suggests an early formation of the faint end similar to the bright red sequence galaxies. De Propris et al. (2013) proposed that the discrepancy is primarily caused by surface brightness selection effects, which lowers the detectability of faint galaxies at high redshift. Nevertheless, a recent study by Martinet et al. (2017) extensively investigated the effect of surface brightness dimming with 16 CLASH clusters in the redshift range of $0.2 < z < 0.6$. They concluded that surface brightness dimming alone could not explain the observed redshift evolution of the faint end. Other possible explanations of the discrepancy invoke the radial and mass dependence of the faint red sequence population, both of which are also debated among local cluster LF studies (see, e.g. Popesso et al. 2006; Barkhouse et al. 2007; Lan et al. 2016). While there may be a (weak) dependence of red sequence LF on cluster mass (or cluster properties that are mass proxies) at intermediate redshift (e.g. De Lucia et al. 2007; Muzzin et al. 2007; Rudnick et al. 2009; Martinet et al. 2015), it remains unclear whether this effect exists at higher redshift. It is also possible that the disagreements in the literature are driven by the large cluster-to-cluster variations, sample selections or the methods used to derive the LF, as observed in most of the abovementioned works.

Resolving the faint end evolution is a crucial step to disentangle the underlying physical processes that quench star formation in cluster galaxies. Mechanisms that can suppress star formation can be broadly classified into those that act internally to the galaxy and often correlate with mass ('mass-quenching'), and external processes that correlate with the environment where the galaxy resides ('environment-quenching'). Examples of mass-quenching mechanisms include feedback from supernovae, stellar winds (for low-mass galaxies, e.g. Dekel & Silk 1986; Hopkins et al. 2014) or active galactic nuclei (AGN) (for more massive galaxies, e.g. Bower et al. 2006; Hopkins et al. 2007; Terrazas et al. 2016), and heating processes that relate to the galaxy halo ('halo-quenching', Dekel & Birnboim 2006; Cattaneo et al. 2008; Woo et al. 2013). On top of these mechanisms that are applicable to all galaxies, a galaxy can also be quenched when it enters dense environments such as galaxy groups and clusters (see Boselli & Gavazzi 2006, 2014,

for reviews). As a galaxy enters a massive halo, its supply to cold gas from the cosmic web is cut off (and may also be accompanied by the stripping of hot gas in the outer parts), which results in a gradual decline of star formation as the fuel slowly runs out ('strangulation' or 'starvation', Larson et al. 1980; Balogh et al. 1997). Quenching can also happen due to rapid stripping of the cold gas in the galaxies when it passes through the intracluster medium (ICM) ('ram pressure stripping', Gunn & Gott 1972) or due to gravitational interactions between galaxies to other group or cluster members, or even the parent halo ('galaxy harassment', e.g. Moore et al. 1998). In the local Universe, it has been shown that the effect of mass and environmental quenching mechanisms are separable (e.g. Peng et al. 2010) and that ram-pressure stripping is able to effectively suppress star formation in cluster galaxies (e.g. Boselli et al. 2016; Fossati et al. 2018). At high redshift, the situation is more complicated. Recent works have shown a mass dependence in the environmental quenching efficiencies at $z \gtrsim 1$ (Cooper et al. 2010; Balogh et al. 2016; Kawinwanichakij et al. 2017; Papovich et al. 2018), which suggest that the effects from both classes are no longer separable. This points to a possible change in the dominant environmental quenching mechanism at high redshift (Balogh et al. 2016). A promising candidate that is supported by recent observations is the 'overconsumption' model (McGee et al. 2014), which suggests the gas supply in the galaxies may be exhausted by the combination of star formation and star-formation-driven outflows. Constraining the evolution of the faint end of the cluster red sequence at high redshift is therefore important to understand the quenching mechanism and its mass dependence.

In this paper we investigate the rest-frame H-band luminosity functions of the red sequence galaxies in seven clusters of the Gemini Observations of Galaxies in Rich Early Environments survey (GOGREEN, Balogh et al. 2017) at $1.0 < z < 1.3$. The GOGREEN survey is an ongoing imaging and spectroscopic survey targeting 21 known overdensities at $1.0 < z < 1.5$ that are representative of the progenitors of the clusters we see today. One of the main science goals of GOGREEN is to measure the effect of environment on low-mass galaxies. Hence, the survey aims at obtaining spectroscopic redshifts for a large number of faint galaxies down to $z' < 24.25$ and $[3.6] < 22.5$, using the Gemini Multi-Object Spectrographs (GMOS) on the Gemini North and South telescopes. Combining all the available redshifts on these overdensities, by the end of the survey we expect to have a statistically complete sample down to stellar masses of $M_* \gtrsim 10^{10.3} M_\odot$ for all galaxy types. The design of the survey and the science objectives, as well as the data reduction are described in detail in Balogh et al. (2017).

The primary goal of this paper is to quantify the faint end of the red sequence LF and to investigate its evolution with redshift in order to shed light on the growth of the faint red sequence galaxies. This paper is organised as follows. A summary of the GOGREEN observations and data used in this paper are described in Section 2. In Section 3 we describe the procedure to derive membership of the galaxies, as well as the techniques used to construct the red sequence luminosity functions. We present the luminosity functions and compare them with a low redshift sample in Section 4. We then compare our results with other cluster samples in the literature and the field in Section 5. In Section 6 we draw our conclusions.

Throughout the paper, we assume the standard flat cosmol-

ogy with $H_0 = 70$ km s^{-1} Mpc^{-1}, $\Omega_\Lambda = 0.7$ and $\Omega_m = 0.3$. Magnitudes quoted are in the AB system (Oke & Gunn 1983).

2. SAMPLE AND DATA

2.1. *The GOGREEN Survey and Observations*

The cluster sample used in this paper is a subsample of the clusters observed in the GOGREEN survey (Balogh et al. 2017). The full GOGREEN sample consists of three spectroscopically confirmed clusters from the South Pole Telescope (SPT) survey (Brodwin et al. 2010; Foley et al. 2011; Stalder et al. 2013), nine clusters from the Spitzer Adaptation of the Red-sequence Cluster Survey (SpARCS, Wilson et al. 2009; Muzzin et al. 2009; Demarco et al. 2010a), of which five were followed up extensively by the Gemini Cluster Astrophysics Spectroscopic Survey (GCLASS, Muzzin et al. 2012), and nine group candidates selected in the COSMOS and Subaru-XMM Deep Survey (SXDS) fields.

In this study we focus on seven GOGREEN clusters at $1.0 < z < 1.3$. The properties of the clusters are summarised in Table 1. Four of the clusters (SpARCS1051, SpARCS1616, SpARCS1634, SpARCS1638) were discovered using the red-sequence technique (Wilson et al. 2009; Muzzin et al. 2009; Demarco et al. 2010a). The remaining three clusters were discovered via the Sunyaev-Zeldovich effect signature from the SPT survey (Bleem et al. 2015). These seven clusters are chosen for their available spectroscopic coverage (from GOGREEN, SpARCS, GCLASS, and the abovementioned SPT works), so that the location of their cluster red sequence can be reliably determined. In this paper we include GOGREEN redshifts for these clusters determined from the spectra taken up to semester 2018A ($\sim 77\%$ project completion).

The spectroscopic information allows us to estimate the halo mass and radius of the clusters using dynamical methods. The procedure of deriving these properties will be described in detail in a forthcoming paper (Biviano et al., in prep.). In brief, using all available redshifts of these clusters, the cluster membership of the spectroscopic objects and velocity dispersions σ_v are determined using the `Clean` algorithm (Mamon et al. 2013) and the new `C.L.U.M.P.S.` algorithm (Munari et al., in prep.). Both algorithms identify cluster members based on their location in projected phase-space, but while the `Clean` algorithm is based on a dynamical model for the cluster, the `C.L.U.M.P.S.` algorithm is based on the location of gaps in velocity space. The cluster M_{200} is derived from the derived velocity dispersion of the clusters using the $M_{200} - \sigma_v$ scaling relation of Evrard et al. (2008).

We found that the M_{200} value of SPT0205 is a factor of ~ 3 lower than the value obtained by the Sunyaev-Zel'dovich effect (SZE) analysis of Ruel et al. (2014). One possible explanation of this is an uncorrelated large-scale structure along the line-of-sight leading to an increase in the SZE signal, especially for low-mass clusters (Gupta et al. 2017). Line-of-sight structures that are dynamically unrelated to the cluster will not be selected by the spectroscopic membership procedures, thus they would not affect the velocity dispersion estimate. However, this explanation is unlikely accurate because the SZ-derived mass is similar to the mass derived from X-ray observations by Bulbul et al. (2019) - if anything, X-ray derived masses tend to underestimate true cluster masses (Rasia et al. 2012). An alternative explanation for the discrepancy between the dynamical and SZ mass estimates is triaxiality. Saro et al. (2013) have shown that the scatter in the mass estimate from

a scaling relation with the velocity dispersion is $\sim 150\%$ at $z \sim 1.3$, and the scatter is mostly due to triaxiality. If SPT0205 is a very elongated cluster and if it is observed with its major axis aligned on the plane of the sky, the observed line-of-sight velocity dispersion would be much lower than the spherically averaged velocity dispersions, thereby leading to a significant underestimate of the mass via the scaling relation. Nevertheless, we have checked that using the SZ mass estimates for this cluster instead of the dynamical estimate will not change our conclusions.

To derive the LF we make use of the deep GMOS z' and *Spitzer* IRAC 3.6 μm images of the clusters. The details of the observation and data reduction of the images are described in Balogh et al. (2017). Below we give a brief summary of the data used in this study.

The z'-band imaging of the clusters were obtained using GMOS-N and GMOS-S imaging mode during September to October, 2014 and March to May 2015. The southern clusters were observed with the Hamamatsu detector of GMOS-S with a typical exposure time of 5.4ks, while the northern clusters were observed with the e2v dd detector of GMOS-N with a long exposure time of 8.9ks to compensate for the lower sensitivity of the e2v detector. The GMOS imaging covers a field of view (FOV) of $5\rlap.'5 \times 5\rlap.'5$. The data were reduced with the Gemini IRAF packages with an output pixel scale of $0\rlap.''1458$ (e2v) or $0\rlap.''16$/pix (Hamamatsu), and the zero-points were determined through comparing with pre-existing CFHT/MegaCAM z' imaging from SpARCS and CTIO/MOSAIC-II z' imaging from the SPT collaboration. The IRAC data of the clusters come from the GCLASS (van der Burg et al. 2013) and SERVS (Mauduit et al. 2012), as well as PI programmes (PI: Brodwin, programme ID 70053 and 60099). Available IRAC data for each cluster were combined to a $10' \times 10'$ mosaic with a pixel scale of $0\rlap.''2$ per pixel using USNO-B as the astrometry reference catalogue.

Before deriving the photometric catalogues, we first register the WCS of z'-band images to the 3.6 μm mosaics. The WCS of the z' images are fine-tuned using GAIA in the Starlink library (Berry et al. 2013) by comparing the coordinates of unsaturated and unblended sources on the z' images to the WCS calibrated 3.6 μm mosaics. The z' images are then resampled to the same grid as the 3.6 μm mosaics using SWarp (Bertin et al. 2002).

2.2. *Source detection and PSF-matched Photometry*

To measure the color of the galaxy accurately, one has to make sure the measured fluxes in different bands come from the same physical projected region. We therefore PSF-match the z' images to the resolution of the 3.6 μm images. For each z' and 3.6 μm image a characteristic PSF is created by stacking bright unsaturated stars. The seeing of the z' images, as measured from the FWHM of the PSFs, varies between $\sim 0\rlap.''6 - 0\rlap.''8$ among the clusters. The FWHM of the 3.6 μm PSFs is $\sim 1\rlap.''8$. With these PSFs we compute the matching kernels to degrade the z' images to the 3.6 μm using the PHOTUTILS package in Astropy (Astropy Collaboration et al. 2013). We check that the ratios of the growth curves of the convolved z' PSF fractional encircled energy to the 3.6 μm PSF deviate by $< 1\%$ from unity.

Source detection and PSF-matched photometry are then performed by running SExtractor (Bertin & Arnouts 1996) in dual image mode. Although the IRAC channel is the redder band, its large-FWHM point spread function (PSF) complicates source detection due to source blending issues. Hence

here we use the unconvolved z'-band image as the detection band. SExtractor is set to detect sources which have three adjacent pixels that are $\geq 1.5\sigma$ relative to local background. Spurious detections at the boundary of the images and those at regions that have variable background due to presence of saturated bright stars (see Figure 1 in Balogh et al. 2017) are removed from the catalogue.

We use aperture magnitudes ($2''$ in diameter) from the PSF-matched z' images and 3.6 μm images for $z' - [3.6]$ color measurements. For galaxy total magnitudes, instead of using the heavily blended 3.6 μm photometry we compute a pseudo-total 3.6 μm magnitude using the abovementioned $z' - [3.6]$ color, the z'-band MAG_AUTO measurement from the unconvolved z'-band image and an aperture correction. The Kron-like MAG_AUTO measures the flux within an area that is 2.5 times the Kron radius (Kron 1980), which is determined by the first moment of the source light profile. It is known that MAG_AUTO misses a small fraction of the source flux ($\sim 5\%$), especially for faint sources for which the integrated area is shrunk to its minimum allowable limit (which is set to the SExtractor default $R_{\min} = 3.5$). To correct for this, we compute an aperture correction following the method described in Labbé et al. (2003) and Rudnick et al. (2009, 2012). We first derive the z'-band growth curve of stars in each cluster by stacking bright unsaturated stars in the unconvolved z'-band images out to $\sim 7\rlap{.}''5$. The correction needed for each galaxy is then computed by comparing its MAG_AUTO aperture area with the growth curve. The median value of the correction for bright galaxies ($18.5 < [3.6] < 20.0$) is ~ -0.03 mag, while for faint galaxies ($22.0 < [3.6] < 23.5$) the median correction increases to ~ -0.10 mag. Note that this is only a first-order correction as it assumes the objects are point sources.

All magnitudes are corrected for galactic extinction using the dust map from Schlegel et al. (1998), and $E(B-V)$ values from Schlafly & Finkbeiner (2011) and those we computed with the filter responses. Stars are identified in the z' band using the SExtractor stellarity parameter (class_star ≥ 0.99) and a color cut ($z' - [3.6] < -0.14$) and are flagged in the catalogue.

To measure the completeness limit of the catalogues, we inject simulated galaxies (hereafter SGs) into the unconvolved z'-band images and attempt to recover them using the same SExtractor setup. For each image, we inject 15000 SGs (10 at a time) with surface brightness profiles described by a Sérsic profile (Sersic 1968), convolved with the z'-band PSF. The SGs are uniformly distributed within a total magnitude range of $20.0 < z' < 27.5$ and have similar structural parameter distributions (n, R_e, q) as observed galaxies at $z \sim 1$, taken from van der Wel et al. (2014). The SGs are distributed randomly in image regions that are not masked by the segmentation map from SExtractor, so that the centroids of the SGs do not directly overlap with existing sources. The recovery rate of these SGs by SExtractor gives an empirical measure of the completeness of our catalogues. We take the magnitude that corresponds to a 90% recovery rate as the completeness limit.

We also measure the formal 5σ depth of the 3.6 μm images using the procedure of the empty aperture simulation described in Labbé et al. (2003). We randomly drop 1000 non-overlapping circular apertures on the image regions where no object resides. The standard deviation of the measured fluxes of these apertures gives an empirical estimation of the uncertainty in the sky level. Using various aperture sizes, we derive a relation between aperture sizes and the measured uncertainties.

The catalogue completeness limits and the formal 5σ limits of our $2''$ aperture magnitudes computed with the relation are listed in Table 1. We use both of the limits to determine the magnitude limit for deriving the LFs (see Section 3.2 for details).

3. CONSTRUCTING THE LUMINOSITY FUNCTION

In this section we describe the technique used to construct the red sequence luminosity functions (LFs) for the GOGREEN sample. The spatial extent of the cluster LFs are limited by the FOV of our GMOS imaging data. After excluding regions with lower S/N, such as the image boundaries and the regions affected by vignetting, the GMOS z' images allow us to measure LF for all seven clusters up to a maximum physical radius of ~ 1 Mpc from the cluster center before losing area coverage. This is larger than R_{200} for the five lower-mass clusters in our sample (see Table 1). To facilitate comparison with the low redshift sample (see Section 3.6), in this paper we mainly present cluster LFs that are computed within a physical radius of $R \leq 0.75$ Mpc, as limited by the low redshift sample. Hence all figures below, unless otherwise specified, are plotted with quantities within $R \leq 0.75$ Mpc. Choosing this radius limit also has the advantage of avoiding some image artifacts in the z' data, which are due to saturated bright stars that are primarily located at the outer part of the images. We also construct LFs computed within radii of $R \leq 0.5R_{200}$, $R \leq 0.5$ Mpc and $R \leq 1.0$ Mpc and will discuss them where applicable. As we will show later, our main conclusion is not sensitive to the choice of the radius limit.

3.1. *Cluster membership*

To construct cluster luminosity functions, it is essential to separate red-sequence galaxies that are truly cluster members from foreground or background interlopers. The ideal way is obviously to get spectroscopic redshifts for all the galaxies in the FOV and perform dynamical analysis to determine their cluster membership (see Section 2.1). However this is very expensive for the faintest galaxies. Although the deep GOGREEN spectroscopy allows us to measure redshifts down to magnitudes $[3.6] < 22.5$, other techniques have to be employed to determine the membership of fainter galaxies or those that are not covered in the spectroscopic sample due to spatial incompleteness.

In this study we determine the membership of the galaxies using a statistical background subtraction technique demonstrated in various works (e.g. Aragon-Salamanca et al. 1993; Stanford et al. 1998; Smail et al. 1998; Andreon 2006; Rudnick et al. 2009, 2012). This technique relies on comparing galaxy number counts of the cluster catalogue with a 'control' field catalogue. Ideally, this field catalogue should have the same depth and should contain identical passbands as the cluster catalogue. Through comparing the catalogues in observed color-magnitude space, the excess in number counts can be converted into a probability of being a cluster member. Other works have also utilised a photometric-redshift techniques, which uses the probability distribution of photometric redshifts to select cluster members (e.g. De Lucia et al. 2004; Pelló et al. 2009). Rudnick et al. (2009) (hereafter R09) have demonstrated that at least for red-sequence galaxies, the statistical background subtraction technique gives consistent results in comparison to those computed using accurate photometric redshifts. This technique allows us to make full use of the deep GOGREEN z' and [3.6] photometry here, at the same time without needing to derive photometric redshifts.

TABLE 1
SUMMARY OF THE IMAGING OF THE GOGREEN CLUSTERS USED IN THIS STUDY IN ORDER OF REDSHIFT.

Full Name	Name	Redshift	σ_v[a] (kms^{-1})	M_{200} ($10^{14}M_\odot$)	R_{200} (Mpc)	Filter	$[3.6]_{\rm lim}$[b] (5σ, AB)	Comp. limit[c] (AB)	Mag limit[d] (AB)
SpARCS J1051+5818	SpARCS1051	1.035	689 ± 36	$2.1^{+0.3}_{-0.3}$	0.9 ± 0.1	GN /z', [3.6]	24.48	25.1	−20.20
SPT-CL J0546−5345	SPT0546	1.067	1016 ± 71	$6.5^{+1.4}_{-1.3}$	1.2 ± 0.1	GS /z', [3.6]	24.12	24.7	−20.51
SPT-CL J2106−5844	SPT2106	1.132	1068 ± 90	$7.2^{+2.0}_{-1.7}$	1.2 ± 0.1	GS /z', [3.6]	23.68	25.0	−20.74
SpARCS J1616+5545	SpARCS1616	1.156	767 ± 38	$2.7^{+0.4}_{-0.4}$	0.9 ± 0.1	GN /z', [3.6]	24.46	25.0	−20.93
SpARCS J1634+4021	SpARCS1634	1.177	715 ± 37	$2.1^{+0.3}_{-0.3}$	0.9 ± 0.1	GN /z', [3.6]	25.09	25.1	−20.89
SpARCS J1638+4038	SpARCS1638	1.196	564 ± 30	$1.0^{+0.2}_{-0.2}$	0.7 ± 0.1	GN /z', [3.6]	25.18	25.2	−20.85
SPT-CL J0205−5829	SPT0205	1.320	678 ± 57	$1.7^{+0.5}_{-0.4}$	0.7 ± 0.1	GS /z', [3.6]	23.87	25.1	−21.53

[a] The velocity dispersions are measured using our dynamical analysis. See Section 2.1 for details.
[b] The quoted 5σ limits are for 2″0 aperture magnitudes.
[c] The 90% completeness limit of the photometric catalogues, derived from the GMOS z'-band images. See Section 2.2 for details.
[d] The cluster absolute magnitude limits in rest-frame H-band, used to derive the LFs. See Section 3.3 for details.

The photometric redshifts will be derived in the near future after we complete acquiring the multiwavelength imaging of the GOGREEN clusters.

3.1.1. *Control field catalogue*

For the 'control' field sample we utilise the publicly available deep Subaru/HSC optical (z) and NIR imaging (y) data in the COSMOS field from the Hyper Suprime-Cam Subaru Strategic Program (HSC-SSP) team and the University of Hawaii (UH) (Tanaka et al. 2017; Aihara et al. 2018), as well as the IRAC 3.6 μm data from the S-COSMOS survey (Sanders et al. 2007). The UltraDeep layer of the HSC-SSP survey is the only publicly available survey that reaches depths comparable to our z'-band data and has a large area to overcome the effects of cosmic variance. Due to the outstanding red sensitivities of the GMOS Hamamatsu and e2v dd detectors and the transmission of the z' filters, the GMOS z'-band has a longer effective wavelength than the HSC z-band. Hence we used both the z and y-band data of HSC-SSP to match the passband of the GMOS z'-band (see Appendix A for a comparison of the transmission of the filter passbands).

To ensure that the photometry of the 'control' field is comparable to our clusters, we have constructed our own 'control' field catalogues using the same method as the clusters. We start by PSF-matching the HSC z and y-band deepCoadd images of the HSC-SSP UltraDeep layer in COSMOS (Tract UD9813) (see Bosch et al. 2018, for details on the HSC-SSP coadd images) to the resolution of the 3.6 μm data. We then align the images and run SExtractor in dual image mode to detect sources and perform photometry, again using the unconvolved z-band as the detection band. Since a single tract of the HSC imaging is split into multiple patches, SExtractor is run on individual patches; the output catalogues are then visually checked to remove spurious detections and are combined into a single master catalogue. For each galaxy we derive an aperture correction to convert MAG_AUTO to a total magnitude using a stacked growth curve of bright unsaturated stars in the corresponding patch. Patches that have depth shallower than our GMOS data or are affected by bright saturated stars and image artifacts were excluded. The final field catalogue contains ∼ 450000 galaxies and covers an area of 1.03 deg^2.

3.1.2. *Membership probabilities*

We adopt the method used in Pimbblet et al. (2002) and R09 to statistically compare the galaxy number counts between the cluster and the field sample. In brief, for each cluster

we construct the $z' - [3.6]$ vs [3.6] color–magnitude diagram and the equivalent color–magnitude diagram for the field. A color term is derived using SSP models to match the filter passbands between the cluster (z') and field (z, y) catalogue (see Appendix A for details).

The cluster galaxy population that satisfies the area selection (e.g. $R \leq 0.75$ Mpc) and the field sample are binned in color–magnitude space with bins of 0.5 mag both in color and [3.6] magnitude. The number counts of the field in each bin are then scaled to the same area selection used for the cluster. By comparing the cluster and field galaxy number counts in each bin, we can assign a cluster membership probability ($P_{\rm memb}$) to each galaxy in the cluster sample. Spectroscopically confirmed cluster members as determined from dynamical analysis (see Section 2.1) are pre-assigned to have a probability of 1. Similarly, confirmed interlopers are pre-assigned to have a probability of 0. The probabilities of the rest of the galaxies in each bin are then assigned as:

$$P_{\rm memb} = 1 - \frac{F_A\, N_{\rm field} - N_{\rm interloper}}{N_{\rm cluster} - N_{\rm interloper} - N_{\rm specmemb}} \quad (1)$$

where F_A is the scaling factor to scale the area coverage of the field to the area of the cluster in consideration. $N_{\rm field}$ and $N_{\rm cluster}$ are the number of galaxies of the field and cluster sample in that particular bin, where $N_{\rm interloper}$ and $N_{\rm specmemb}$ correspond to the number of spectroscopically confirmed interlopers and cluster members, respectively. From Equation 1 one can also see that the probability will not be well defined if $F_A\, N_{\rm field} > (N_{\rm cluster} - N_{\rm specmemb})$. To solve this we follow the approach of Pimbblet et al. (2002) to expand the color and magnitude selection used to calculate this probability by merging neighbouring bins until the resultant probability reaches $0 \leq P_{\rm memb} \leq 1$.

Note that the total sum of probabilities within a bin (or, equivalently, the effective number of cluster members $N_{\rm eff}$) is always set by statistical background subtraction. The numbers of both confirmed members and interlopers are folded in Equation 1, so that the membership probability of the rest of the galaxies in the bin would be adjusted accordingly to conserve the total sum of probabilities.

To derive the uncertainty of the background subtraction, instead of computing the probability by rescaling the entire COSMOS catalogue, we perform the same process with randomly selected regions in the catalogue with the same area as the cluster. This allows us to derive the resultant 1σ field-

to-field variation within COSMOS. In addition, we derive the uncertainty in the number of galaxies of the COSMOS field sample due to cosmic variance, following the recipe in Moster et al. (2011). The two uncertainties are added in quadrature, and the combined uncertainty is then used as the uncertainty of the probabilities.

3.2. *Red sequence selection*

The red sequence galaxies of the cluster sample are identified using $z' - [3.6]$ vs $[3.6]$ color magnitude relations (CMR). We fit the CMR for each cluster using a fixed slope of -0.09. Due to the low contrast of the cluster red sequence against interlopers, only spectroscopically confirmed galaxies that have no visually identifiable [O II] emission lines are used to derive the fit. The chosen slope of -0.09 is determined by fitting the CMR of SpARCS1616 and SPT0546, the two clusters that have a large number of spectroscopically confirmed galaxies, which allows us to reliably determine the slope and the zero-point simultaneously. We note that this is also the same slope of the CMR found in De Lucia et al. (2004, 2007) and R09. The potential red sequence galaxies are selected as galaxies within ±0.25 mag of the fitted CMRs. Since some of the clusters have only a small number of spectroscopically confirmed members, we use a fixed magnitude selection for all the clusters. The 0.25 mag selection corresponds to $\sim 1.5 - 2.0\sigma$ of the intrinsic scatter of the fitted CMRs. We verify that varying the slope by ±0.1 (i.e. 0.01, −0.19) or increasing the red sequence selection to ±0.4 mag do not change our main conclusion.

We also identify the brightest cluster galaxy (BCG) in each cluster using a simple ranking system. Three scores are assigned to each galaxy according to a) its [3.6] total magnitude (score: 3 if $[3.6] \leq 18.5$, 2: $18.5 < [3.6] \leq 19.5$, 1: $19.5 < [3.6] \leq 20$), b) distance to the cluster centroid (3: $R \leq 0.25$ Mpc, 2: $0.25 < R \leq 0.5$ Mpc, 1: $0.5 < R \leq 1.0$ Mpc) and c) $z' - [3.6]$ color (3: $z' - [3.6] >$ CMR−0.5, 2: CMR−1.5 $< z' - [3.6] \leq$ CMR-0.5, 1: $0 \leq z' - [3.6] \leq$ CMR-1.5. The highly-scored candidates (with a total score ≥ 4) are then visually examined to determine the most probable BCG. In most clusters, the BCG can be clearly identified. The candidate BCG is usually the brightest confirmed cluster member in [3.6] within the uncertainties, except in SpARCS1634, where there exists one other member that is significantly off-centered (~ 500 kpc) and is brighter in [3.6] than the assigned BCG. We test that choosing this galaxy as the cluster BCG instead does not change our conclusion.

Figure 1 shows the color magnitude diagram of the GOGREEN clusters and their fitted CMRs. The zero-point (ZP) of the CMR at $[3.6] = 0$ is given in each panel. Note that at the time of writing this paper the data acquisition for GOGREEN is still ongoing, hence some of the clusters show a lack of spectroscopic members at faint magnitudes. The fully-completed GOGREEN spectroscopic sample will be complete down to $[3.6] < 22.5$. The magnitude limit of each cluster is set to be the brighter magnitude between its 90% completeness limit (after converting into [3.6] using the red sequence color) and the 5σ limit of the 3.6 μm image. We find that for all the GOGREEN clusters the magnitude limit is set by the 90% completeness limit.

3.3. *Deriving the red sequence luminosity function*

At $1.0 < z < 1.3$, the 3.6 μm images correspond roughly to rest-frame H-band. We derive k-correction factors using

Bruzual & Charlot (2003) stellar population models and the software EzGal (Mancone & Gonzalez 2012) to convert the [3.6] into rest-frame H-band magnitudes. We assume a model with a formation redshift of $z_f = 3.0$, $Z = Z_\odot$ and a Chabrier (2003) initial mass function (IMF). We have checked that this model is able to reproduce the red sequence color of the clusters at their particular redshifts. The k-corrections range from ~ -0.71 to -0.89 depending on the redshift of the cluster. The absolute magnitude limit of the clusters in rest-frame H-band is listed in Table 1.

Assuming the observed cluster LF can be described by a single Schechter (1976) function $\Phi(M)$, we construct the LF and derive the Schechter parameters for each cluster, including the characteristic magnitude M^*, the faint end slope α that characterises the power-law behaviour at magnitudes fainter than M^*, and the normalisation Φ_* using two different approaches:

1. The binning method. Based on the cluster membership probabilities we computed in Section 3.1, we derive 1000 Monte Carlo realizations of the red sequence sample for each cluster. The red sequence realizations are binned in rest-frame H-band absolute magnitudes with a 0.5 mag bin width to the cluster magnitude limit. The LF is then derived by taking the average of the number of galaxies of the realizations in each magnitude bin.

   The error budget of each magnitude bin of the LF comprises the Poisson noise on the number of galaxies in the bin, computed using the recipe of Ebeling (2003), and the uncertainty of the background subtraction (i.e. from the membership probabilities).

   The binned LFs are fitted with a single Schechter (1976) function. Since the Schechter parameters are highly degenerate, we follow the χ^2 grid fitting approach described in R09, which samples the parameter space and reduces the chance of the fit trapping in some local χ^2 minima. We start by constructing a coarse grid of ϕ_*, M_H^*, α. The Poisson error of each bin is first symmetrized, the χ^2 value at each grid point is evaluated, and a finer grid is then constructed using the set of parameters that give the lowest χ^2 as the new centroid of the grid. This process is iterated for two more times to derive the best-fit. For each grid point we convert the χ^2 value into a probability with $P = \exp(-\chi^2/2)$. The 1σ uncertainty of each parameter is then determined through marginalising the other two parameters to obtain a probability distribution and taking the bounds that encloses the 16% and 84% of the probability distribution.

2. The maximum likelihood estimation (MLE) method. We also derive the LF using a parametric maximum likelihood estimator. The standard MLE method (i.e. the STY method), first proposed by Sandage et al. (1979), has been used in various LF studies. In this paper we use a modified MLE approach to account for the cluster membership probabilities. The best fit is found by maximising the following log-likelihood function:

$$\ln \mathcal{L} = \sum_{i=1}^{N} \left(P_{\mathrm{memb,i}} \times \ln P(M_i) \right) \tag{2}$$

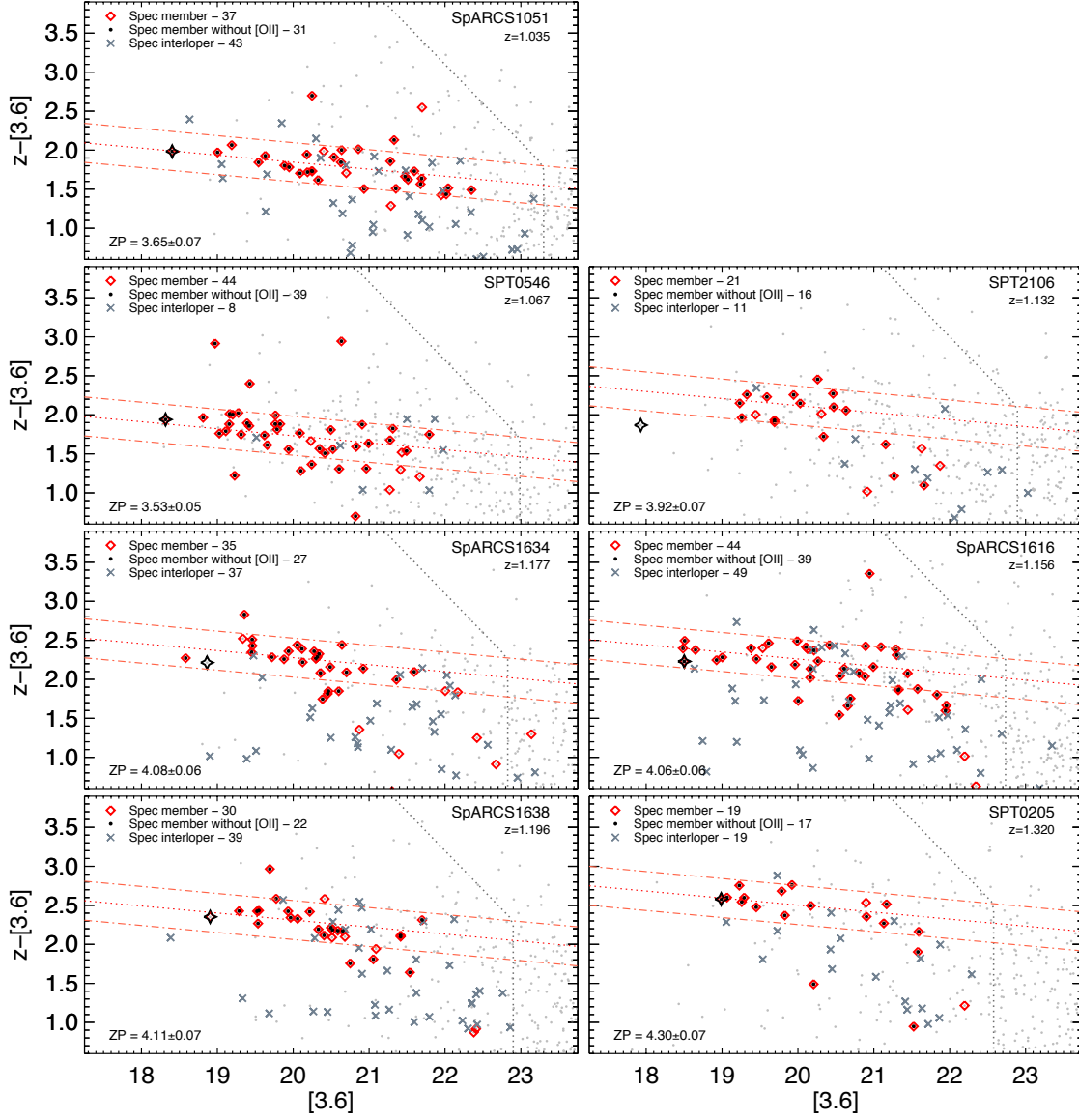where $P_{\mathrm{memb,i}}$ is the cluster membership probability for

FIG. 1.— Color–magnitude diagram of the seven GOGREEN clusters used in this study in order of increasing redshift. The photometry is described in Section 2.2. The red diamonds correspond to spectroscopically confirmed cluster members. Passive members that do not have obvious [O II] emission are marked in black. The dark grey crosses mark the interlopers, and the black star symbol corresponds to the BCG of the clusters. The red dotted line in each panel corresponds to the fitted CMR. The dotted-dashed lines in each panel correspond to ±0.25 mag from the fitted relation, which is the region we used for our red sequence selection. The dark grey dotted lines mark the magnitude limit of each cluster (see Section 3.2 for details). The zero-point (ZP) of the CMR at [3.6] = 0 is given in each panel. It can be seen that the fixed slope we adopt (−0.09) describes the CMR of all the clusters well.

each galaxy described in Section 3.1, and $P(M_i)$ is the probability of observing a galaxy of absolute magnitude M_i according to the Schechter (1976) function:

$$P(M_i) \propto \frac{\Phi(M_i)}{\int_{-\infty}^{M_{\rm lim}} \Phi(M) dM} \qquad (3)$$

The upper limit $M_{\rm lim}$ is set to be the magnitude limit for each cluster. Note that strictly speaking this method also involves binning of the data as well, as $P_{\rm memb,i}$ is derived in binned color-magnitude space. $P_{\rm memb,i}$ is incorporated into Equation 2 in a way such that it is equivalent to running Monte Carlo realizations of the MLE derivation with the probabilities. To estimate the uncertainty of the Schechter parameters of the fit we

follow the prescription described in Marchesini et al. (2007) to determine the error contours of M^* and α from the values of the log-likelihood. The 68%, 95%, and 99% confidence level are estimated by finding the ellipsoids that satisfy $\ln \mathcal{L} = \ln \mathcal{L}_{\rm max} - 0.5\chi_\beta^2(2)$ where $\chi_\beta^2(2) = 2.3, 6.2, 11.8$, respectively. To propagate the uncertainty of the membership probabilities due to field-to-field variation within COSMOS and cosmic variance, we also derive 500 Monte Carlo realizations of the red sequence probabilities and repeat the MLE fit. The 1σ variation of the best-fit Schechter parameters from these realizations is then added in quadrature with the above-mentioned uncertainty of the Schechter parameters. In all cases, the 1σ variation of the Schechter parameters due to the uncertainty of the probabilities is much smaller than the uncertainty of the Schechter parameters

of the fit.

In both methods we exclude the BCG and galaxies brighter than the BCG when constructing the LF, as is common practice.

3.4. *Composite red sequence luminosity function*

The number of galaxies in the LFs of high redshift clusters is often too low to reliably determine Schechter parameters. Hence beside individual cluster LFs we also derive composite red sequence LF by combining the sample to measure cluster average properties. Before stacking the LFs, a passive evolution correction is applied to the rest-frame absolute magnitudes M_H to bring all clusters to the mean redshift of the sample at $\bar{z} \sim 1.15$. This correction is again computed using Bruzual & Charlot (2003) stellar population models ($z_f = 3.0$, $Z = Z_\odot$ and a Chabrier (2003) IMF). The corrections range from ~ -0.05 to 0.13 depending on the redshift of the cluster. Similar to Section 3.3, the composite LF is also derived and fitted with both the binning approach and the MLE approach.

For the former approach, we adopt the method of Colless (1989) to combine individual cluster LFs into a single composite. The Colless (1989) method combines individual LFs by renormalising the bin counts with the total number of galaxies in each LF down to a certain renormalisation magnitude limit (i.e. to convert the number counts in a particular magnitude to a fraction of the sample) and summing these renormalised counts. Therefore the cluster LFs are normalised to the same effective richness before being combined into a single composite. The renormalisation magnitude limit has to be brighter than the magnitude limits of all the clusters being stacked, and, at the same time faint enough so that the total number of galaxies used for renormalisation is representative of the richness of the clusters (Popesso et al. 2005). For our GOGREEN sample the renormalisation magnitude limit is chosen to be $M_H = -21.5$. We then fit the composite LF down to the brightest magnitude of the magnitude limits of the individual clusters.

For the MLE approach, we derive the best-fitting Schechter function using the entire red sequence sample and their corresponding cluster membership probabilities down to the same magnitude limits as the binning approach. Similar to the individual cluster LF, we derive 500 Monte Carlo realizations of the red sequence probabilities using the uncertainty of the membership probabilities and repeat the MLE fit. The 1σ variation of the best-fit Schechter parameters from these realizations is then added in quadrature with the fitting uncertainties, and the combined uncertainty is used as the uncertainty of the Schechter parameters. We present the composite LFs derived with both approaches in Section 4.

3.5. *Faint-to-luminous Ratio*

Another quantity that is commonly used in previous studies to describe the luminosity distribution of red sequence galaxies, is the faint-to-luminous ratio (or dwarf-to-giant ratio). The faint-to-luminous ratio is simply the ratio of the number of faint galaxies within a certain magnitude range to the number of those brighter than this faint population. Essentially being a two-bin LF, the faint-to-luminous ratio is a simple quantity that is easy to compute and compare straightforwardly with other samples, without needing to assume any functional form of the underlying galaxy luminosity distribution (Gilbank & Balogh 2008).

Here we adopt the definition of the faint-to-luminous ratio as in De Lucia et al. (2004, 2007) to enable a comparison with earlier works. Luminous red sequence galaxies are defined as galaxies with rest-frame V-band Vega magnitude $M_{V,\text{vega}} \leq -20$, and faint red sequence galaxies are those with $-20 < M_{V,\text{vega}} \leq -18.2$. We apply k-corrections and evolution corrections to the z'-band total magnitudes of our red sequence sample to convert them into rest-frame V-band magnitude at $z = 0$. The corrections are again computed using BC03 models, assuming $z_f = 3.0$ and $Z = Z_\odot$. The combined corrections (not including the distance moduli) range from ~ -1.35 to -1.12 depending on the redshift of the cluster.

Similar to the LF we compute the ratio for regions within a radius of $R \leq 0.75$ Mpc. For all clusters except SPT0205, we run 10000 random realisations of the red sequence sample using the cluster membership probabilities from Section 3.1.2, varying also the galaxy magnitudes within their uncertainties. Following the above definition, we then compute the faint-to-luminous ratio for each realisation, and take the median and the 1σ scatter of the distribution as the cluster faint-to-luminous ratio and its associated uncertainty. This method is not applicable to SPT0205, as its rest-frame V-band depth (converted from z'-band) is not deep enough to compute the number of faint galaxies. Hence for SPT0205 we first derive the rest-frame V-band LF and its best-fitting Schechter function using the same red sequence selection and fitting method described in Section 3.3. The only difference is that the LF is derived in rest-frame V-band instead of H-band. We then integrate the best fit down to -18.2 to extrapolate the number of faint galaxies for the faint-to-luminous ratio. The uncertainties of the Schechter parameters are propagated to the computed ratio. Due to the large uncertainty of the Schechter fit, the faint-to-luminous ratio computed in this way has a considerably larger uncertainty.

We also compute the cluster-average faint-to-luminous ratio for the entire sample by integrating the best fitting Schechter function of the rest-frame V-band composite LF.

3.6. *Low redshift comparison sample*

As we mentioned in the introduction, one of the primary goals of this work is to investigate the evolution of the red sequence LF with redshift. Several works have demonstrated that using different filter passbands, methods to determine cluster membership, and procedure to construct LF can affect the derived Schechter parameters to a large extent (see, e.g. Alshino et al. 2010). Therefore to ensure the comparison is accurate, we decide to construct our own low-redshift comparison instead of comparing our results to LF derived in previous works.

The low redshift comparison sample we used in this study is from the ESO Distant Cluster Survey (EDisCS, White et al. 2005), which targets optically selected cluster fields in the redshift range of $0.4 < z < 1.0$ from the Las Campanas Distant Cluster Survey (LCDCS, Gonzalez et al. 2001). The rest-frame g,r and i-band red sequence LFs of sixteen EDisCS clusters are studied in detail in R09. To avoid wavelength-dependent effects and possible biases due to the procedure used, we re-derive cluster LFs using the EDisCS photometric and spectroscopic catalogues (White et al. 2005; Halliday et al. 2004; Milvang-Jensen et al. 2008; Pelló et al. 2009, R09) with filter bands that are comparable in rest-frame wavelength with our GOGREEN sample. The EDisCS photometric catalogue comprises photometry in either B, V, I, K_s or V, R, I, J, K_s-bands from VLT/FORS2 and NTT/SOFI depending on the

redshift of the cluster. To mimic the $z' - [3.6]$ selection used for the GOGREEN sample, we identify red sequence candidates through fitting the CMR in $R - K_s$ vs K_s (or $V - K_s$ vs K_s if R-band is not available) for clusters with $z < 0.57$. For higher redshift clusters the CMR is fitted in $I - K_s$ vs K_s. Among the cluster sample in R09, we exclude the clusters CL1354-1230 and CL1059-1253 as they have insufficient depth in the K_s-band image, hence we arrive at a sample of fourteen clusters. The properties of the clusters can be found in Table 2. We have checked that the choice of the color does not largely impact the red sequence selection. For most clusters selecting with $R - K_s$ or $I - K_s$ color gives consistent results.

To determine the cluster membership probabilities we follow the statistical background subtraction method outlined in Section 3.1. For the EDisCS clusters the COSMOS/UltraVISTA catalogue (DR1, Muzzin et al. 2013a) is used as the control field catalogue. The UltraVISTA photometry are derived in a similar way as the EDisCS clusters. The large area coverage (~ 1.8 deg^2) and the photometric bands, including the optical ($u^*, g^+, r^+, i^+, z^+, B_j, V_j$ + 12 medium bands) and deep NIR (Y, J, H, K_s) photometry make it the perfect candidate for this purpose. Note that this is a different field sample as the one used in R09 as we are measuring the LF in K_s-band.

We then apply k-corrections and evolution corrections to convert the K_s magnitudes to rest-frame H-band magnitudes at the mean redshift of the selected EDisCS clusters ($\bar{z} \sim 0.60$), and derive rest-frame H-band composite LFs following the same procedure and fitting methods described in Section 3.3 and 3.4. Instead of using the EDisCS catalogue completeness limit ($I \sim 24.9$) as the magnitude limit for fitting the LF, we measure 5σ magnitude limits of the V, R, I, K_s bands from the uncertainties of the galaxies in the photometric catalogues and compute the corresponding magnitude limits in rest-frame H-band. We found that the K_s-band magnitude limit is always the brightest among all the bands, thus it is used as the magnitude limit for fitting the LF. Note that the K_s-band limits ($K_s \sim 21.0 - 22.3$) are also brighter than the completeness limit converted to K_s-band using the $I - K_s$ color of the red sequences ($\sim 1.0 - 2.5$).

4. RESULTS

In this section we present the red sequence LFs of the GOGREEN clusters. We will start by presenting the red sequence LF of individual clusters, followed by the composite LFs and the comparison with the low redshift sample. For simplicity, the LFs are shown in galaxy number counts ($\log(N)$) in all figures.

4.1. *Individual luminosity function*

Figure 2 shows the red sequence LF of the seven GOGREEN clusters. The binned LFs are plotted to the respective cluster magnitude limits. In general, the measured binned LFs can be described reasonably well by a single Schechter function. For SpARCS1616, the apparent excess of galaxies that are brighter than the BCG is caused by the bright galaxies with comparable brightness with the BCG (see Figure 1) and the choice of binning. On the other hand, the excess in SpARCS1634 is a result of an off-center galaxy that is brighter than the assigned BCG (see Section 3.2 for details).

In all the clusters there is a gradual decrease of the number of red sequence galaxies towards the faint end, which is also reflected in the derived αs: all seven clusters show $\alpha \gtrsim -0.8$.

TABLE 2
SUMMARY OF THE PROPERTIES OF THE 14 EDisCS CLUSTERS USED FOR COMPARISON.

Name	Redshift	M_{200}[a] ($10^{14} M_\odot$)	R_{200} (Mpc)	Filter[b]	Mag limit[c] (AB)
CL1216-1201	0.794	$7.6^{+1.7}_{-1.6}$	$1.4^{+0.1}_{-0.1}$	I, K_s	-20.97
CL1054-1245	0.750	$1.0^{+0.8}_{-0.3}$	$0.7^{+0.2}_{-0.1}$	I, K_s	-20.55
CL1040-1155	0.704	$0.6^{+0.3}_{-0.2}$	$0.6^{+0.1}_{-0.1}$	I, K_s	-20.79
CL1054-1146	0.697	$1.6^{+0.7}_{-0.5}$	$0.9^{+0.1}_{-0.1}$	I, K_s	-20.81
CL1227-1138	0.636	$1.5^{+0.6}_{-0.5}$	$0.9^{+0.1}_{-0.1}$	I, K_s	-20.81
CL1353-1137	0.588	$2.4^{+1.8}_{-1.2}$	$1.0^{+0.2}_{-0.2}$	I, K_s	-20.61
CL1037-1243	0.578	$0.3^{+0.2}_{-0.1}$	$0.5^{+0.1}_{-0.1}$	I, K_s	-20.63
CL1232-1250	0.541	$10.6^{+3.9}_{-2.4}$	$1.7^{+0.2}_{-0.1}$	V, K_s	-20.53
CL1411-1148	0.519	$3.1^{+1.9}_{-1.4}$	$1.2^{+0.2}_{-0.2}$	V, K_s	-20.76
CL1420-1236	0.496	$0.1^{+0.1}_{-0.1}$	$0.4^{+0.1}_{-0.1}$	V, K_s	-20.68
CL1301-1139	0.483	$2.8^{+1.1}_{-0.9}$	$1.1^{+0.1}_{-0.1}$	V, K_s	-20.56
CL1138-1133	0.480	$3.4^{+1.1}_{-1.0}$	$1.2^{+0.1}_{-0.1}$	R, K_s	-20.12
CL1018-1211	0.474	$1.0^{+0.4}_{-0.3}$	$0.8^{+0.1}_{-0.1}$	V, K_s	-20.50
CL1202-1224	0.424	$1.3^{+0.8}_{-0.6}$	$0.9^{+0.2}_{-0.2}$	V, K_s	-19.92

[a] The cluster M_{200} is estimated using the $M_{200} - \sigma_v$ relation from Evrard et al. (2008). The σ_v are taken from the EDisCS photometric catalogues.
[b] The bands we used to fit the cluster CMR for red sequence selection.
[c] The cluster absolute magnitude limits in rest-frame H-band, used to derive the LFs. See Section 3.6 for details.

We find that the binning approach and the MLE approach give consistent estimates of Schechter parameters. In all clusters the derived α and M_H^* from both methods are consistent within 1σ. The best-fitting Schechter parameters of the MLE method (α, M_H^*) and the effective number of red sequence galaxies ($N_{\rm eff,RS}$) that goes into the LF derivation for each cluster are given in Table 3. Note that due to statistical background subtraction, the effective number of red sequence galaxies in each cluster is no longer an integer.

4.2. *Composite luminosity function*

In Figure 3 we show the composite red sequence LF of the seven GOGREEN clusters. The LFs of individual clusters are corrected to the mean redshift of the sample at $\bar{z} \sim 1.15$ before stacking. Note that the BCGs have been removed before deriving the LF.

The bright end of the LF appears to be well described by the exponential part of the Schechter function. Previous studies at lower redshifts have reported an excess of red sequence galaxies at the bright end that deviates from the best fitting Schechter function (e.g. Biviano et al. 1995; Barrena et al. 2012; Martinet et al. 2015). Although part of the excess seen in previous works is due to the fact that these works included the cluster BCGs in the LF, the excess has been shown to be made up by bright red sequence galaxies that are not BCGs (see e.g. Barrena et al. 2012; Cerulo et al. 2016). We do not find evidence of such excess in the composite GOGREEN LF, although the bright end of our composite LF has large uncertainty due to the small number of bright galaxies we have in the sample (and small number of clusters) and the variation in the number of bright galaxies among the clusters.

By combining the sample as a whole, we can constrain the cluster-average α and M_H^* simultaneously with higher accuracies. The measured composite LF shows a prominent decline at the faint end, with best fitting Schechter parameters $\alpha \sim -0.35^{+0.15}_{-0.15}$ and $M_H^* \sim -23.52^{+0.15}_{-0.17}$ from the MLE method and $\alpha \sim -0.23^{+0.12}_{-0.08}$ and $M_H^* \sim -23.47^{+0.11}_{-0.10}$ from the χ^2 grid
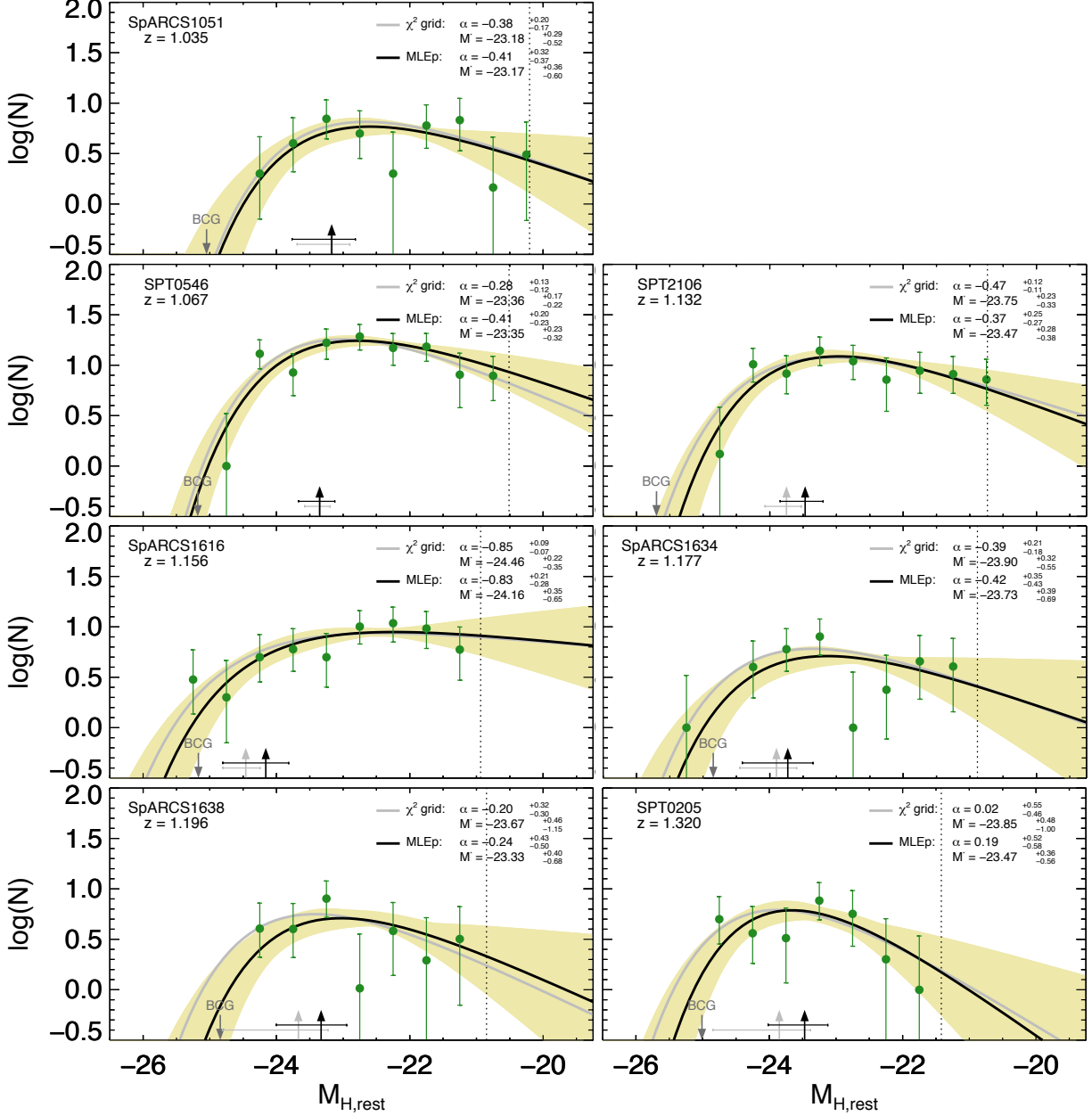
FIG. 2.— Rest-frame H-band red sequence LF of the seven GOGREEN clusters included in this study. The grey line in each panel shows the best-fit Schechter function to the binned LF points using the χ^2 grid approach. The black line corresponds to the best-fit estimated from the MLE method. The yellow shaded region represents 1σ uncertainties of the LF estimated from the MLE method. The vertical black dotted lines denote the absolute H-band magnitude limit used for fitting the LF. The best fitting M_H^* of both methods and their 1σ uncertainties are denoted by the vertical arrows and the horizontal error bars.

method.[1] In the section below when comparing α and M_H^* among samples we will mainly refer to those derived from the MLE method, as they give more conservative results.

We also study the halo mass dependence and cluster-centric radial dependence of the composite LF. The results are shown in Appendix B and C. We see no obvious dependence of Schechter parameters on halo mass, but there may be a hint of a radial dependence, in a way that the LF in the inner 0.5 Mpc

show a more positive α than the outer region $0.5 < R \leq 1.0$ Mpc.

We have also investigated the potential effect of source blending in our photometry and verified that source blending is unlikely to affect our conclusions. The tests and results are described in Appendix D.

4.3. Comparison with low redshift sample

In this section we examine the redshift evolution of the cluster red sequence by comparing our results to the EDisCS sample at $\bar{z} = 0.60$. Before comparing their LFs, we first check if the two samples are comparable in mass. Various studies have shown that there are possible correlations between the LF parameters and cluster mass (e.g. Popesso et al. 2006; Martinet et al. 2015), it is therefore important to also take into account
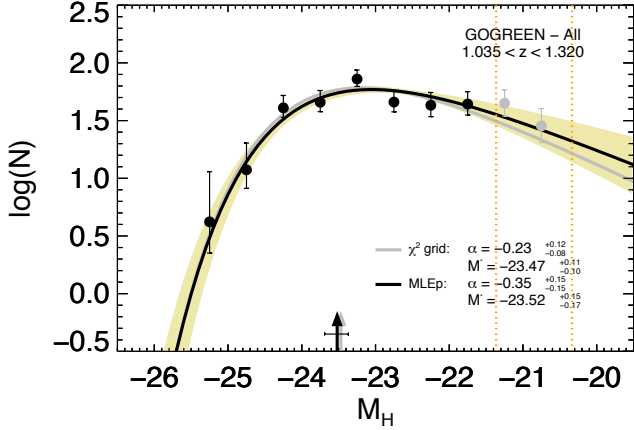
---

[1] Note that both fits are fitted down to the brightest magnitude of the magnitude limits of the individual clusters. If the extra two data points that are within the range of magnitude limits are included in the χ^2 grid fit (as permitted by the Colless (1989) method for stacking LF with different limits), we find that the resultant $\alpha \sim -0.42^{+0.06}_{-0.06}$ and $M_H^* \sim -23.63^{+0.08}_{-0.10}$ differ by $> 1\sigma$ with the above χ^2 grid fitting results, but are consistent within 1σ of the MLE method.

FIG. 3.— Composite rest-frame H-band red sequence LF of the seven GOGREEN clusters. Passive evolution correction have been applied before stacking to bring all the clusters to the mean redshift of the sample ($\bar{z} \sim 1.15$). The orange dotted lines bracket the range of the absolute M_H magnitude limits (after corrected to $\bar{z} \sim 1.15$) of the seven clusters. The data points show the stacked LF using the Colless (1989) method. Points that are within the magnitude limits of all the clusters are shown in black and those that are within the range of magnitude limits are shown in grey. The grey line shows the best-fit to the LF (black points) using the χ^2 grid approach. The black line corresponds to the best-fit estimated from the MLE method. The yellow shaded region represents 1σ uncertainties of the LF estimated from the MLE method. Vertical arrows and horizontal error bars of the same color show the corresponding best-fit M_H^* and 1σ uncertainty.
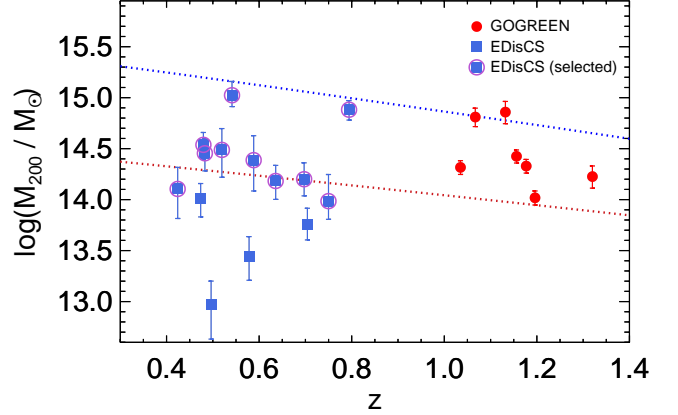

FIG. 4.— Halo masses of the GOGREEN and EDisCS clusters. The blue and red dotted lines show the expected halo mass history of the most massive EDisCS cluster CL1232-1250 and the least massive GOGREEN cluster SpARCS1638, computed using the concentration-mass relation and mass accretion history code (COMMAH, Correa et al. 2015a,b,c). It can be seen that given the expected halo mass histories, ten of the EDisCS clusters (circled) are plausible descendants of the GOGREEN clusters.

the growth of the cluster when comparing clusters at different redshifts.

Figure 4 shows the halo mass of the clusters in the two samples with redshift. We also plot the expected halo mass accretion history of the most massive EDisCS cluster (CL1232-1250) and the least massive GOGREEN cluster (SpARCS1638), computed using the concentration-mass relation and mass accretion history code (COMMAH, Correa et al. 2015a,b,c). COMMAH uses the extended Press-Schechter formalism (e.g. Bond et al. 1991; Lacey & Cole 1993) to compute the average halo mass accretion history for a halo with a given initial mass at a certain redshift. Note that here we merely use the expected halo mass histories of the two clusters as a reference. Due to the stochastic nature of structure formation, there is considerable scatter in the average mass accretion history (~ 0.2 dex at $z \sim 1$ as seen in simulations e.g. van den Bosch et al. 2014) that is not included in the analytical models.

Given the expected growth, it can be seen that while most of the EDisCS sample are plausible descendants of the GOGREEN clusters within the uncertainties, four of the clusters may have halo masses that are too low to compare with the GOGREEN sample. Therefore, in addition to the comparison with all fourteen EDisCS clusters, we also compose a subsample that comprises only the plausible descendants of the GOGREEN clusters (marked with circles in Figure 4), for which we refer to as the selected EDisCS clusters below. Overall, we find that comparing the GOGREEN clusters to all EDisCS clusters or the subsample that is restricted to plausible descendants results in consistent conclusions. For completeness, the results of both comparisons are shown and discussed below.

The comparison of the composite LF of the GOGREEN clusters to all the EDisCS clusters and to the selected EDisCS clusters is shown in Figure 5 and Figure 6, respectively. We have corrected the GOGREEN LFs for passive evolution to $z = 0.60$ to account for the fading of the stellar population. The correction is again computed using BC03 SSP, assuming

a formation redshift of $z_f = 3$ and solar metallicity. In order to trace the redshift evolution of the LF, a correction to the normalisation of the GOGREEN LF is also needed so that the (relative) number counts of the two samples can be compared directly. In Figure 5 and 6 we have rescaled the evolution corrected GOGREEN LF in three different ways, such that it has the same total luminosity density, number of clusters and total halo mass at $z = 0.6$ as the EDisCS LFs, respectively. In previous works the LFs being compared are often rescaled to have total luminosity density. This is, however, only useful in comparing the shape (i.e. α and M_H^*) of the LFs as it provides no information on the evolution in absolute galaxy numbers. One way is to rescale with the number of clusters as shown in the bottom left panel, but the results can be biased by the mass distribution of the samples even if the samples have been shown to be plausibly evolutionarily linked.

Despite the fact that we have twice as many clusters in the EDisCS sample as in GOGREEN, the mean M_{200} of the EDisCS sample ($2.7 \pm 0.5 \times 10^{14} M_\odot$) is lower than the mean M_{200} of GOGREEN ($3.3 \pm 0.3 \times 10^{14} M_\odot$) before even taking into account the growth of the cluster mass over the redshift range. Similarly, the mean M_{200} ($3.5 \pm 0.7 \times 10^{14} M_\odot$) of the selected EDisCS clusters is already comparable to the GOGREEN sample.[2] It is therefore potentially problematic to rescale the LF using solely the ratio of the number of clusters in the EDisCS and GOGREEN samples in our case, as the difference in the mass distributions in the samples might lead to incorrect conclusions. To solve this we rescale the GOGREEN LF using the ratio of the total halo mass of the two samples at $z = 0.6$ (bottom right panel in both figures). The expected average halo mass of the GOGREEN sample at $z = 0.6$ ($7.0 \times 10^{14} M_\odot$) is again estimated with COMMAH. This is essentially halo-mass matching the samples and comparing their LFs per unit halo mass. Comparing with the result that rescales with number of clusters, it can be seen that rescaling with halo-mass gives a smaller normalisation, which is due to the fact

---

[2] We note that the mean M_{200}s of the full EDisCS sample and the selected EDisCS cluster subsample are comparable within 1σ with GOGREEN. Nevertheless, this will not be true at $z = 0.6$ as GOGREEN clusters will grow by a factor ~ 2.1 according to the expected halo mass accretion history from COMMAH.

that GOGREEN clusters are on average more massive than EDisCS clusters.

From Figure 5, it is clear that the bright ends of the GOGREEN and EDisCS LFs are consistent with each other after we correct for the passive evolution of the GOGREEN clusters to the EDisCS redshift and halo-mass match the two samples. This suggests that the bright red sequence population in the cluster is mostly in place already at $z \sim 1$. We can also see from Figure 6 that restricting the sample to only plausible descendants gives consistent results.

The faint end, on the other hand, shows an evolution from $z \sim 1.15$ to $z \sim 0.60$. This is evident from the lack of red sequence galaxies fainter than M_H^* in the GOGREEN LF compared to the EDisCS LF. Since the two Schechter parameters α and M_H^* are degenerate, in Figure 7 we show the likelihood contours for both parameters from the MLE approach. It can be seen that there is a $> 3\sigma$ level difference between the Schechter parameters of the evolution corrected GOGREEN sample and both EDisCS samples. Marginalising the parameters suggests the difference primarily comes from α, while the evolution corrected M_H^* of the two LFs are well consistent within 1σ and show no evolution.

Our result of an evolving α with redshift is consistent with recent studies by Zhang et al. (2017) and Sarron et al. (2018) at lower redshift ranges. Zhang et al. (2017) studied the red sequence LF for a sample of X-ray selected clusters from the Dark Energy Survey at $0.1 < z < 1.05$ and reported a $\sim 1.9\sigma$ redshift evolution in the faint end slope. Sarron et al. (2018) studied the evolution of the LF of both early-type and late-type galaxies in clusters at $z \leq 0.7$ and found an increase in faint galaxies in both populations with decreasing redshift. Our result is also consistent with the 'downsizing' scenario (Cowie et al. 1996) of red sequence formation seen in low redshift clusters (e.g. Nelan et al. 2005; Smith 2005; Smith et al. 2012), such that faint red-sequence galaxies become quiescent at a later time than the bright massive ones.

Besides LFs that are computed within a physical radius of 0.75Mpc, we also compare GOGREEN and EDisCS LFs that are computed within $0.5R_{200}$. We find the same conclusion as found using $R \leq 0.75$Mpc, that the bright ends of the two $0.5R_{200}$ LFs are consistent with each other, and that the faint end slope shows an evolution from $z \sim 1.15$ to $z \sim 0.60$. The best-fitting Schechter parameters are given in Table 3.

4.4. *The total red sequence luminosity*

To quantify the build up of the faint end of the red sequence, in this section we measure the growth of the total luminosity of the red sequence over time.[3] We integrate the best fitting LFs of the GOGREEN and the full and selected EDisCS samples, as well as the individual cluster LFs. To make sure the conclusion is not affected by the extrapolation of the LF, we have also integrated the LFs down to the magnitude limit of the EDisCS sample ($M_H \leq 21$). The results are consistent with the complete integrals.

Figure 8 shows the total red sequence luminosity L_{RS} of the samples. Without any corrections, the measured values of the red sequence luminosity of the GOGREEN clusters are higher than both the full and selected EDisCS cluster samples (top panel). After accounting for the fading of the stellar

population with the passive evolution correction and rescaling the GOGREEN LF using the ratio of the total halo mass of the full and selected EDisCS samples (as in bottom right panel of Figure 5 and 6), in the middle and bottom panels we see an evolution in the (mean) red sequence luminosities between the GOGREEN sample to the EDisCS samples. Taking into account the uncertainties, the red sequence luminosities only grow by $\sim 31\% \pm 30\%$ (full EDisCS sample, $\sim 13\% \pm 28\%$ if we consider the selected EDisCS sample) over the ~ 2.6 Gyrs between $z \sim 1.15$ and $z \sim 0.60$.

It is not surprising that the growth of red sequence luminosities between the two samples is not significant, as we have shown that the bright end of the LF, which constitutes the majority of the red sequence light, is fully assembled in the GOGREEN sample. If we split the red sequence luminosities at $M_H = -23$ (passive evolution corrected), which roughly corresponds to M_H^* of both samples at $z \sim 0.60$, we find that the mean luminosity of the bright end ($M_H \leq -23$) of the GOGREEN clusters is consistent with EDisCS ($\sim -13\% \pm 31\%$ (full), $\sim -24\% \pm 29\%$ (selected), pluses in Figure 8), albeit with considerable uncertainty. On the other hand, the faint end ($M_H > -23$) of the GOGREEN sample needs to grow by almost a factor of 2 ($\sim 104\% \pm 39\%$ (full), $\sim 76\% \pm 35\%$ (selected)) in luminosity to meet the EDisCS sample (crosses).

Our result that the bright end is already assembled by $z \sim 1.15$ is consistent with van der Burg et al. (2015), in which they compared the stellar mass density distributions of $z \sim 1$ GCLASS clusters, four of which are also in the sample used in this work, to a sample of low redshift clusters ($0.04 < z < 0.26$). They found that the central parts ($R < 400$ kpc) of the stellar mass distributions of satellite galaxies in local galaxy clusters are already in place at $z \sim 1$. Here we show that this is also true for red sequence galaxies as the total red sequence luminosity is mostly in place from the contribution of the assembled bright end. Interestingly, there has been evidence showing that even the bright end is still being assembled at higher redshift. For example, Rudnick et al. (2012) derived the red sequence LF of a $z = 1.62$ cluster IRC0218 and found that the bright end of the LF is less populated than its descendants at $z \sim 0.6$ with a factor of two less in the total red sequence luminosity despite the fact that the shape of the LFs are consistent with each other. If IRC0218 is a typical case, this is then consistent with the picture that the massive end evolves faster than the faint end. The massive end completes most of the assembly until $z \sim 1$ and then followed up by the build up of the faint end of the red sequence. Note that this does not mean that the bright end of the red sequence completely stops evolving after $z \sim 1$, as other processes, such as the growth of the BCGs via mergers and the arrival of newly quenched galaxies, will continue to affect the bright end of the red sequence to the present day (see Section 4.5.1 for an estimation of the effect of BCG growth to the total red sequence luminosity).

The comparison here, however, assumes that all red sequence galaxies evolve passively in the same way down to $z \sim 0.60$ and the average growth of the GOGREEN sample is well described by the average mass accretion history, while in reality cluster galaxies and the clusters themselves may have different formation histories. We check that varying z_f in the SSP models introduces ~ 0.1 mag variation in the evolution correction. This corresponds to a ~ 0.05 dex (i.e. $\sim 11-12\%$) systematic uncertainty in the derived mean red sequence luminosities of the GOGREEN clusters and is $\sim 3-4$ times

---

[3] Although we do not convert the total red sequence luminosity to a total mass in this section, we would like to inform the reader that the rest-frame M/L_H at $z = 0.60$ is ~ 0.63, as derived from SSP model assuming $z_f = 3.0$ and $Z = Z_\odot$.
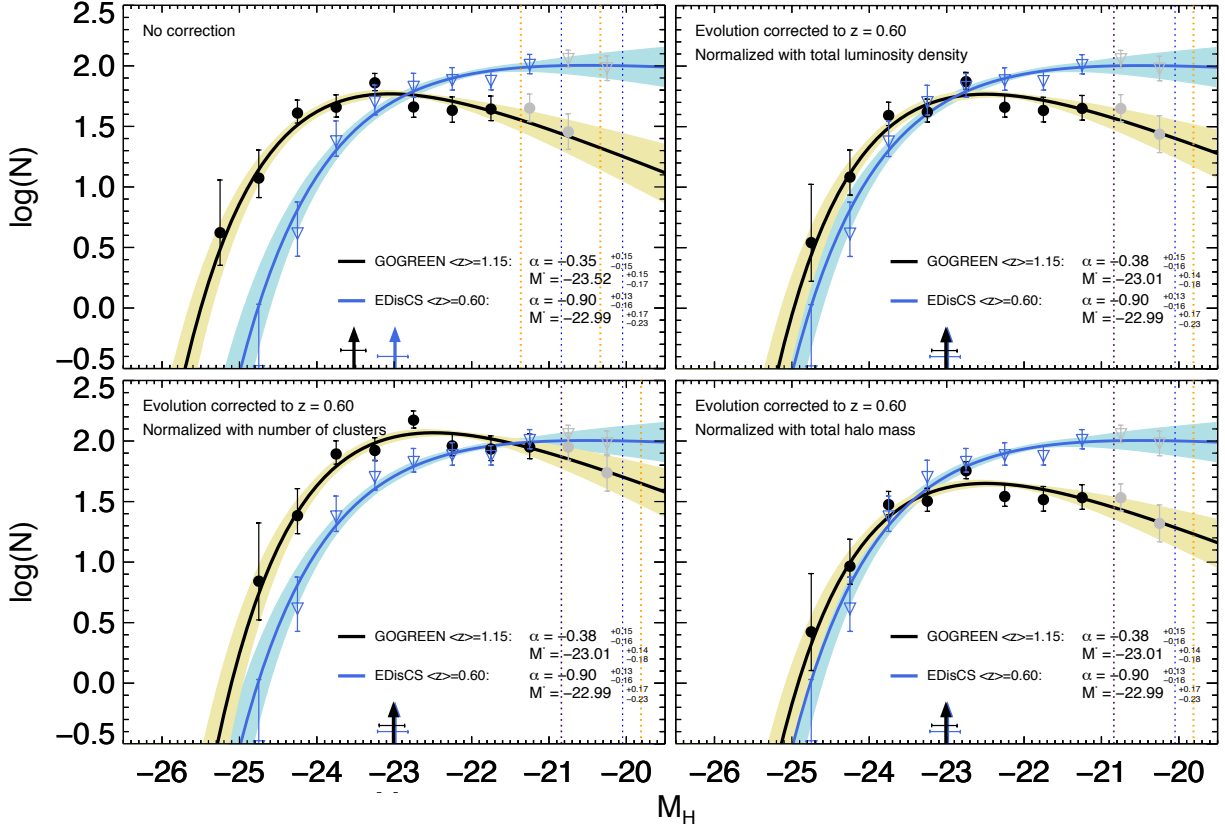
FIG. 5.— Composite rest-frame H-band red sequence LF of GOGREEN and EDisCS clusters. Top left: composite LFs of the two samples at their respective mean redshifts without evolution correction and correction in the normalisation. Top Right: Passive evolution correction has been applied to the GOGREEN clusters to bring them to the mean redshift of the EDisCS sample. The GOGREEN LF and its best-fits are scaled (i.e. shifted vertically) to have the same total luminosity density as the EDisCS LF. Bottom left: same as top right, but the GOGREEN LFs are scaled to have the same number of clusters as the EDisCS sample. Bottom right: same as top right, but the GOGREEN LFs are rescaled to have the same total halo mass at $z \sim 0.6$ as the EDisCS sample. The black and blue lines in all panels correspond to the best-fit Schechter function for the GOGREEN and the EDisCS sample, respectively. Vertical arrows of the same color show the corresponding best-fit M_H^*. The yellow and cyan shaded region represents 1σ fitting uncertainties of the GOGREEN and EDisCS LF. The orange and blue vertical dotted lines bracket the range of M_H magnitude limits of the GOGREEN and EDisCS clusters. Due to the difference in mean M_{200} mass of the two samples, we suggest that the LF should be renormalized with halo mass for comparison (see Section 4.3 for details). It can be seen that there is a lack of red sequence galaxies in the faint end of the GOGREEN LF compared to the EDisCS sample.

smaller than our uncertainties. Note that the LF and the total red sequence luminosity we show here are computed within a physical radius of 0.75Mpc. We also verify that using LFs that are computed within $R \leq 0.5R_{200}$ gives a similar conclusion, in the sense that the majority of the growth in the red sequence luminosity occurs at the faint end.

4.5. Additional caveats
4.5.1. Growth of the BCG and ICL

There are two relevant components that we did not consider in the above comparisons, the growth of the BCG and the intracluster light (ICL). Recent studies on BCG stellar mass growth revealed that BCGs grow by a factor of $\sim 2 - 3$ since $z \sim 1$ primarily via major mergers, although when this growth takes place is still controversial (e.g. Lidman et al. 2012; Lin et al. 2013; Ascaso et al. 2014; Bellstedt et al. 2016). For the ICL, several simulation (e.g. Martel et al. 2012; Contini et al. 2014) and observational works (e.g. DeMaio et al. 2015, 2018) have demonstrated that it originates from the disruption and tidal stripping of massive satellite galaxies of $\log(M/M_\odot) \sim 10 - 11$, and that the majority of the ICL growth happens below $z \sim 1$. Since the BCGs are excluded from our LFs, both the growth of the BCGs and ICL will manifest as a decrease in total red sequence luminosity at low redshift and therefore reduces the observed growth in total red sequence luminosity

between the two samples.

A detailed analysis of the growth of the BCGs between the two samples is out of the scope of this paper, but we can roughly estimate the effect of BCG growth on the total red sequence luminosity using literature values. Using the mean total (aperture) magnitudes of the GOGREEN BCGs[4], we find that on average the luminosities of the GOGREEN BCGs are $\sim 10\%$ ($\sim 3\%$) of the total red sequence luminosities. Hence the growth of the BCGs would corresponds to $\sim 3\%$ ($\sim 1\%$) of the total red sequence luminosity, assuming they grow uniformly in time. Similarly the contribution of the growth of ICL to the red sequence luminosity is also not significant; simulations show that most of the ICL assembles after $z \sim 1$ and its fraction of mass grows from $\sim 5 - 10\%$ to $\sim 30 - 40\%$ of its $z \sim 0$ value between $z \sim 1.15$ and $z \sim 0.60$ (Contini et al. 2014, 2018). They show that the stellar mass growth of the ICL has a BCG mass dependence. The growth can reach ~ 1 BCG mass by $z \sim 0.5$ for more massive BCGs ($\log(M/M_*) > 11.5$, less growth for less massive BCGs). Hence even if we assume all the ICL comes from red sequence galaxies, this still

---

[4] We are aware that the total magnitude is not an accurate measurement of the stellar component of the BCG but includes BCG+ICL, as we did not separate the ICL from the contribution of the outer halo of the BCG, although the BCG accounts for the bulk of the BCG+ICL mass at $z \sim 1$ (Contini et al. 2018). Here we simply use the luminosity of the BCGs to show that the effect of BCG growth to the red sequence luminosity is negligible.
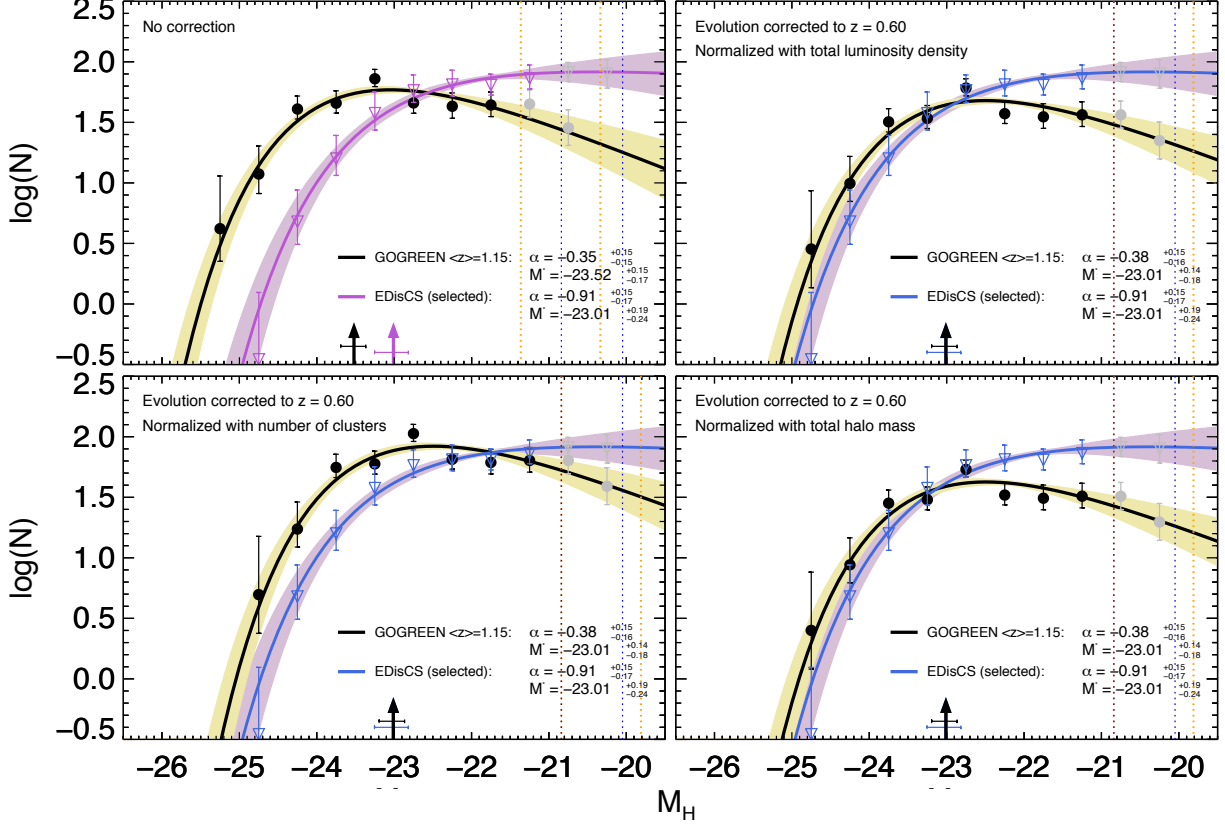
FIG. 6.— Composite rest-frame H-band red sequence LF of GOGREEN and the selected EDisCS clusters. Same as Fig 5, but the composite LF includes only ten clusters in the EDisCS sample that are plausible descendants of the GOGREEN clusters within the uncertainties (violet).

TABLE 3
EFFECTIVE NUMBER OF RED SEQUENCE GALAXIES AND THE DERIVED SCHECHTER PARAMETERS OF THE RED SEQUENCE LFs WITH THE MLE METHOD.

Name	Redshift	$N_{\text{eff,RS}}$[a]	α	M_H^*
	z		(mag)	
SpARCS1051	1.035	37.0 ± 1.3	$-0.41^{+0.32}_{-0.37}$	$-23.17^{+0.36}_{-0.60}$
SPT0546	1.067	104.5 ± 2.1	$-0.41^{+0.20}_{-0.23}$	$-23.35^{+0.23}_{-0.32}$
SPT2106	1.132	71.6 ± 1.8	$-0.37^{+0.25}_{-0.27}$	$-23.47^{+0.28}_{-0.38}$
SpARCS1616	1.156	57.0 ± 1.4	$-0.83^{+0.21}_{-0.28}$	$-24.16^{+0.35}_{-0.65}$
SpARCS1634	1.177	31.4 ± 1.1	$-0.42^{+0.35}_{-0.43}$	$-23.73^{+0.39}_{-0.69}$
SpARCS1638	1.196	29.5 ± 1.7	$-0.24^{+0.43}_{-0.50}$	$-23.33^{+0.40}_{-0.68}$
SPT0205	1.320	27.7 ± 1.5	$0.19^{+0.52}_{-0.58}$	$-23.47^{+0.36}_{-0.56}$
All clusters ($R \leq 0.75$ Mpc)	$1.035 \leq z \leq 1.320$	315.9 ± 3.5	$-0.35^{+0.15}_{-0.15}$	$-23.52^{+0.15}_{-0.17}$
All clusters ($R \leq 0.5R_{200}$)	$1.035 \leq z \leq 1.320$	250.8 ± 2.3	$-0.31^{+0.17}_{-0.18}$	$-23.42^{+0.16}_{-0.19}$
High-mass clusters ($R \leq 0.75$ Mpc)	$1.067 \leq z \leq 1.132$	173.6 ± 2.8	$-0.33^{+0.17}_{-0.17}$	$-23.40^{+0.18}_{-0.23}$
Low-mass clusters ($R \leq 0.75$ Mpc)	$1.035 \leq z \leq 1.320$	163.1 ± 2.6	$-0.43^{+0.19}_{-0.21}$	$-23.67^{+0.20}_{-0.26}$
All clusters ($R \leq 0.5$ Mpc)	$1.035 \leq z \leq 1.320$	214.9 ± 3.5	$-0.17^{+0.19}_{-0.20}$	$-23.38^{+0.17}_{-0.20}$
All clusters ($R \leq 1.0$ Mpc)	$1.035 \leq z \leq 1.320$	334.0 ± 4.6	$-0.32^{+0.15}_{-0.16}$	$-23.47^{+0.14}_{-0.17}$
All clusters ($0.5 \leq R \leq 1.0$ Mpc)	$1.035 \leq z \leq 1.320$	119.2 ± 2.9	$-0.57^{+0.22}_{-0.26}$	$-23.64^{+0.25}_{-0.36}$
EDisCS clusters ($R \leq 0.75$ Mpc)	$0.424 \leq z \leq 0.794$	433.1 ± 5.4	$-0.90^{+0.13}_{-0.16}$	$-22.99^{+0.17}_{-0.23}$
EDisCS clusters (selected) ($R \leq 0.75$ Mpc)	$0.424 \leq z \leq 0.794$	350.8 ± 4.7	$-0.91^{+0.15}_{-0.17}$	$-23.01^{+0.19}_{-0.24}$
EDisCS clusters ($R \leq 0.5R_{200}$)	$0.424 \leq z \leq 0.794$	328.3 ± 4.4	$-0.80^{+0.16}_{-0.18}$	$-22.85^{+0.19}_{-0.23}$
EDisCS clusters (selected) ($R \leq 0.5R_{200}$)	$0.424 \leq z \leq 0.794$	280.1 ± 4.2	$-0.82^{+0.17}_{-0.20}$	$-22.84^{+0.20}_{-0.27}$

[a] The effective number of red sequence galaxies ($N_{\text{eff,RS}}$) are computed by deriving 1000 realizations of the red sequence with the galaxy membership probabilities and calculating the sum of the probabilities in each realizations. $N_{\text{eff,RS}}$ is taken to be the median of the sums of the probabilities in these realizations and its uncertainty is the 1σ variation of the sums.
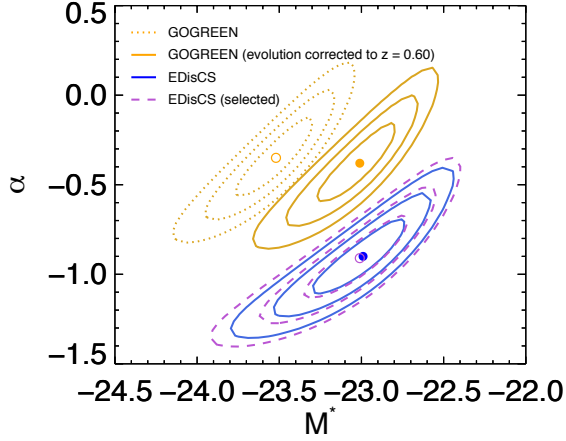
Fig. 7.— The likelihood contours for the Schechter parameters α and M_H^* for the GOGREEN and EDisCS clusters from the MLE approach. Dotted and solid orange lines show the 1,2 and 3σ confidence contours of the two parameters before and after applying evolution correction for the GOGREEN sample. Solid blue and dashed violet lines show the confidence contours of the full EDisCS sample and selected EDisCS cluster sample. The circles correspond to the best fitting Schechter parameters. There is a $> 3\sigma$ level difference between the Schechter parameters of the evolution corrected GOGREEN sample and both EDisCS samples, which primarily comes from α.

corresponds to $< 10\%$ of the total red sequence luminosity.

4.5.2. *Contamination from dusty star forming galaxies*

Another caveat comes from the contamination from dusty star forming galaxies. Our red sequence selection alone is not able to differentiate between quiescent galaxies and star forming galaxies that appear red because of dust extinction. In the last decade, the UVJ color classification, which utilises the rest-frame $U - V$ and $V - J$ colors, has become a popular technique as it is able to separate 'genuine' quiescent galaxies from dusty star-forming ones (e.g. Labbé et al. 2005; Wolf et al. 2005; Williams et al. 2009; Muzzin et al. 2013b). By using the UVJ classification we can estimate the average fraction of contamination in our red sequence, assuming the red sequence selection includes all the UVJ quiescent and dusty star forming galaxies. We utilise the existing multi-band catalogues of the GCLASS clusters and SpARCS clusters at a similar redshift range (i.e. the $0.86 < z < 1.1$ and $1.1 < z < 1.4$ bin of the cluster sample in Nantais et al. 2017). To select dusty star forming galaxies we follow the criterion in Spitler et al. (2014) to select objects in the UVJ star forming region that have $V - J > 1.2$. We also tried the selection in Fumagalli et al. (2014) (i.e. $U - V > 1.5$) and found that the two selection criteria gave consistent results for the clusters.

We find that dusty star forming galaxies contribute to $17\% \pm 6\%$ in number of the total galaxy population (for galaxies with $\log(M_*/M_\odot) \geq 10.3$) at $1.1 < z < 1.4$. For the $0.86 < z < 1.1$ bin the contribution is even lower, with $9\% \pm 9\%$. This, combined with the fact that the quiescent fraction is $\sim 80\%$ at $1.1 < z < 1.4$ and $\sim 85\%$ at $0.86 < z < 1.1$ (Nantais et al. 2017), suggests that the contamination from dusty star forming galaxies can contribute up to $\sim 11 - 20\%$ to our red sequence (at least for $M_H \geq -21.5$ at $z \sim 0.65$, which the above mass limit roughly corresponds to). It is likely that this contamination is even lower in the EDisCS sample, as the quiescent fraction in clusters increase with decreasing redshift and the fraction of dusty star forming galaxies decrease with decreasing redshift (see also Martis et al. 2016, for similar trends in the field). Hence taking this into account will result
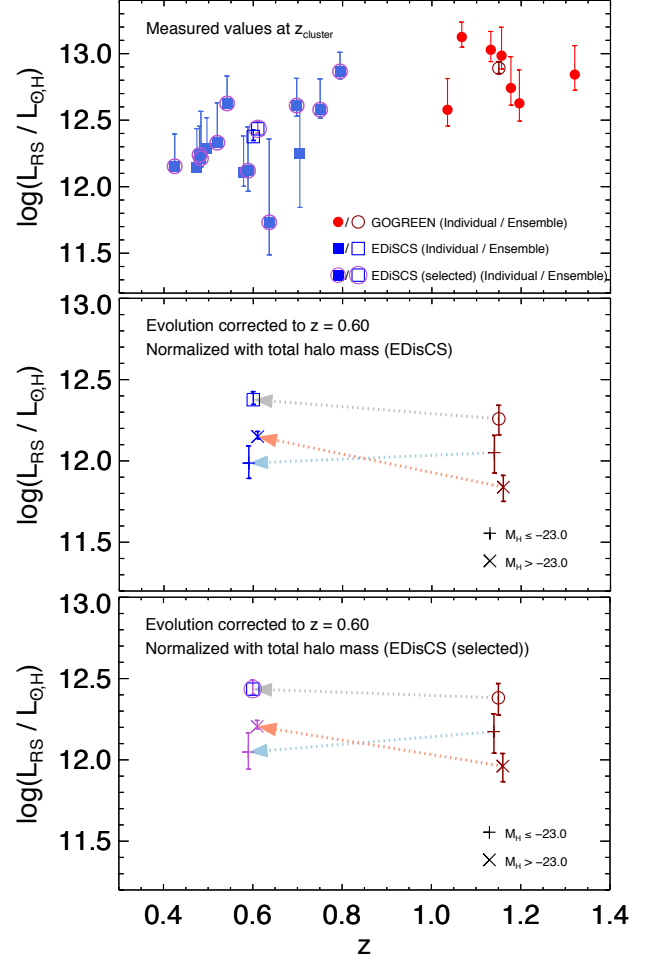

Fig. 8.— Total red sequence luminosity of the GOGREEN and EDisCS clusters. Top: luminosities measured by integrating the LF (without evolution correction) at the respective cluster redshift. Middle: Passive evolution correction has been applied to fade the mean red sequence luminosity of the GOGREEN sample to the mean redshift of the full EDisCS sample, and the mean luminosities of the GOGREEN sample are rescaled to have the same total halo mass at $z \sim 0.6$ as EDisCS. The mean red sequence luminosity of the two samples are derived from the composite LFs. The pluses and crosses correspond to the red sequence luminosity of each sample with $M_H \leq -23.0$ (bright end) and $M_H > -23.0$ (faint end), respectively. Bottom: Same as the middle panel, except that the selected EDisCS sample is used for rescaling. It can be seen that the majority of the growth in luminosity occurs at the faint end of the red sequence.

in an even larger difference between the LF of the two samples than the one we see in Section 4.3 and 4.4.

5. DISCUSSION

By comparing the GOGREEN sample with the EDisCS sample, we have shown that the red sequence cluster LF exhibits an evolution in the faint end slope α from $z \sim 1.15$ to $z \sim 0.60$. The bright end, on the other hand, seems to be mostly in place already by $z \sim 1.15$, which suggests a strong luminosity (or mass) dependence in the build up of the red sequence. With only two samples, however, we are not able to truly trace the redshift evolution of the build up of the faint end. In the following sections we investigate the redshift dependence of the build up of the red sequence and how this build up depends on the environment.

5.1. *The evolution of the cluster faint-to-luminous ratio*

Another analogous way to probe the redshift evolution of the build up of the red sequence is to compare the faint-to-

luminous ratio of clusters in different redshifts. Similar to the faint end slope of the red sequence LF, various works have debated whether there is an evolution of the faint-to-luminous ratio with redshift (see, e.g. Capozzi et al. 2010; Bildfell et al. 2012; Cerulo et al. 2016, and references therein). The left panel of Figure 9 compares the faint-to-luminous ratio of our sample with results from the literature (De Lucia et al. 2007; Stott et al. 2007; Andreon 2008; Stott et al. 2009; Capozzi et al. 2010; Bildfell et al. 2012). To avoid biases due to inconsistent definitions, we only plot values from works that define the faint-to-luminous ratio in a way that is compatible with De Lucia et al. (2007) in Figure 9. Studies that use a different definition due to insufficient depth of the data (e.g. Gilbank et al. 2008; Cerulo et al. 2016) are not included in the comparison. In most cases we use the ensemble-averaged ratio quoted in their works directly, except we have binned the Bildfell et al. (2012) results in redshift bins of $\Delta z = 0.1$. Note that here we do not make any cut in halo mass or other cluster properties and simply include all values that are available.

It is evident from Figure 9 that there is a general trend of decreasing faint-to-luminous ratio with increasing redshift when we compare our results at $z \sim 1.15$ with those at lower redshifts. It is worth noting that similar to the LFs, we also see a decrease in faint-to-luminous ratio in the GOGREEN sample compared to the ratio of the EDisCS clusters (derived by De Lucia et al. 2007). The cluster-average GOGREEN faint-to-luminous ratio ($0.78^{+0.19}_{-0.15}$) is consistent with the expected evolution predicted by Gilbank & Balogh (2008), which assumes a functional form of $(1 + z)^{-1.8 \pm 0.5}$ and is derived through fitting the measured faint-to-luminous ratios of $z \lesssim 0.9$ cluster samples from the literature. Our result is also consistent with the empirical relation predicted by Bildfell et al. (2012), which has a parametrisation of $((0.88 \pm 0.15)z + (0.44 \pm 0.03))$ and is derived from 97 clusters at a redshift range of $0.05 \leq z \leq 0.55$. Although the Gilbank & Balogh (2008) and Bildfell et al. (2012) relations differ by a considerable amount at low redshift (which Bildfell et al. (2012) suggests is due to the way the photometry is measured), they give very similar predictions at $z \sim 1$, hence we are not able to distinguish between the two relations.

The evolution of the faint-to-luminous ratio is simply a change in the proportion between the faint and bright red sequence population. One caveat of using this quantity, as suggested by Crawford et al. (2009), is that it is difficult to ascertain whether the measured evolution is due to the bright end or the faint end of the LF, as a changing M^* can also contribute to the observed evolution in the faint-to-luminous ratio. Nevertheless, in Section 4.4 we show that the bright end of the red sequence has been mostly in place since $z \sim 1$ after we apply the passive evolution correction. Combining this with the fact that the EDisCS LFs also show a similar bright end to that of the SDSS sample (as seen in R09), we can conclude that the evolution in faint-to-luminous ratio since $z \sim 1.15$ is a result of the gradual build up of the faint end of the red sequence. This conclusion is consistent with previous works studying the cluster red sequence at lower redshifts (e.g. De Lucia et al. 2007; Rudnick et al. 2009; Stott et al. 2009; Bildfell et al. 2012; Martinet et al. 2015; Zhang et al. 2017; Sarron et al. 2018).

Despite the clear evolutionary trend, we note that the ratios of our clusters appear to be lower than those of the three $z > 1$ clusters in Andreon (2008), although there seems to be good agreement of their $z < 1$ measurements with the

literature. One possible explanation is that this is simply due to cluster-to-cluster variation, as noted in other studies (e.g. De Lucia et al. 2007; Crawford et al. 2009). The different color selection used in the red sequence selection (*HST*/F775W - F850LP color was used in Andreon (2008), which may be problematic for $z > 1$ clusters as both bands are bluer than the 4000Å break) and methods to measure the ratio may also play a role to the discrepancy. Our result here is also in contrast with Cerulo et al. (2016), who found no evolution in faint-to-luminous ratios (luminous-to-faint ratio in their work) in the red sequence of nine high redshift clusters at $0.8 < z < 1.5$. They reported that the ratios of the high redshift clusters (and the fitted α of the LF) are consistent with the WINGS clusters at $z \sim 0$, albeit with a large scatter. We note that they adopt a different definition of bright and faint galaxies, which is brighter than the one used in De Lucia et al. (2007) due to the insufficient depth of their data. Using the same definition as in Cerulo et al. (2016) we find a faint-to-luminous ratio ($0.81^{+0.12}_{-0.11}$), which is consistent with the one using the De Lucia et al. (2007) definition. This value, after converting to luminous-to-faint ratio, is consistent within 1σ with three out of six of $z > 1$ clusters in the Cerulo et al. (2016) sample. It is possible that the apparent discrepancy is due to the scatter in their high redshift sample, or due to the definition of faint galaxies (i.e. which can suppress the faint-to-luminous ratio in their low redshift comparison point), as the majority of the observed evolution comes from the very faint end of the red sequence.

5.2. *Comparison to the field*

Having established the gradual build up of the faint end of the cluster red sequence over time, we then investigate the environment dependence of this build up by comparing the faint-to-luminous ratio of the clusters to the field. Gilbank & Balogh (2008) performed a similar analysis and compared the cluster faint-to-luminous ratios up to $z \sim 0.9$ to a field sample combining various surveys, including the SDSS (Bell et al. 2003; Baldry et al. 2004), COMBO-17 (Bell et al. 2004), the Millennium Galaxy Catalogue (Driver et al. 2006), COSMOS (Scarlata et al. 2007) and VVDS (Zucca et al. 2006). In this work, we make use of the new COSMOS/UltraVISTA DR3 catalogue (Muzzin et al. in prep.) to construct the faint-to-luminous ratio of the field up to the redshift of the GOGREEN sample. The UltraVISTA DR3 catalogue comprises ~ 50-band optical and infrared photometry and is significantly deeper than the DR1 release. The catalogue covers an area of ~ 0.7 deg^2.[5]

We derive the faint-to-luminous ratios for the field in redshift bins of $\Delta z = 0.2$ using the spectroscopic and photometric redshift information, as well as the rest-frame V-band magnitudes derived using EAZY (Brammer et al. 2008) in the UltraVISTA DR3 catalogue. To select passive galaxies we utilise the UVJ classification used in Muzzin et al. (2013a). Although this is not the same color selection used for the GOGREEN clusters, we stress that the possible systematics resulting from the selection difference will not change the conclusion of the comparison (see Section 4.5.2 for a discussion). We adopt the same definition of the faint-to-luminous ratio as in De Lucia et al. (2004) for the field. To convert the galaxy magnitudes to $z = 0$, we compute an evolution correction for individual galaxies using their stellar population history parameters de-
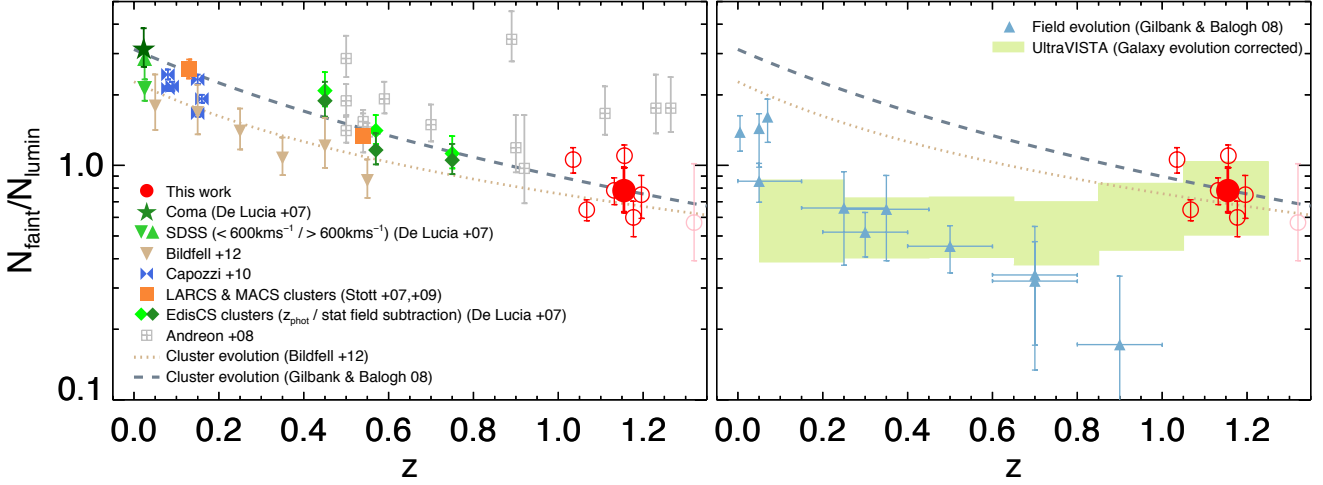
FIG. 9.— The red sequence faint-to-luminous ratio ($N_{\mathrm{faint}}/N_{\mathrm{lumin}}$) of the GOGREEN clusters. Left: Comparison with the literature values of cluster sample at different redshifts. Empty symbols correspond to the ratios of individual clusters (GOGREEN & Andreon 2008), while filled symbols correspond to the ratios deriving from cluster samples (De Lucia et al. 2007; Stott et al. 2007, 2009; Capozzi et al. 2010; Bildfell et al. 2012). Due to insufficient depth of the image, the ratio of SPT0205 is computed using extrapolation of the fitted LF and is shown in pink (see Section 3.5 for details). The red filled circle shows the ratio derived using composite LF of all seven clusters. It is evident that there is a general trend of decreasing faint-to-luminous ratio with increasing redshift up to $z \sim 1.15$. The ratio of the GOGREEN clusters are consistent with the evolution relations derived by Gilbank & Balogh (2008) and Bildfell et al. (2012), respectively. Right: Comparison with the field. The light green shaded regions correspond to the 1σ regions of the field faint-to-luminous ratios derived with the UltraVISTA catalogue, taking into account the variation in the evolution correction from different assumptions (see Section 5.2 for details). The field ratios in Gilbank & Balogh (2008) are shown as blue triangles. It can be seen that clusters at $z \sim 1.15$ have consistent faint-to-luminous ratios as in the field. The ratios in clusters evolve strongly with redshift, while the ratios in the field show a much milder redshift dependence.

rived with FAST (Kriek et al. 2009) in the DR3 catalogue. Using a single formation redshift evolution correction for all the field galaxies is not preferred as the color variation among passive galaxies in the field at a given redshift is much larger than the red sequence in clusters. For each galaxy, we construct a model using the exponential decaying SFH parameters (age, Z, A_V and τ) and passively evolve this model down to $z = 0$ to obtain the correction. Various assumptions in deriving this correction have been tested, such as 1) keeping the same dust extinction at $z = 0$ versus no more dust at $z = 0$ and 2) using a SSP model with the same age (i.e. formation redshift) instead of an exponential decaying SFH. The systematics due to these assumptions are kept as a range of the faint-to-luminous ratios at each redshift bin. Even with the DR3 catalogue the evolution corrected rest-frame V-band depth is not deep enough for computing the number of faint galaxies in the $z \sim 0.95$ and $z \sim 1.15$ bins (~ 0.2 and ~ 0.7 mag brighter than the limit, respectively), primarily due to the large color variation in the field population. Hence for these two bins we follow the method described in Section 3.5 to extrapolate the number of faint galaxies to compute the faint-to-luminous ratio. We have also included the uncertainty from cosmic variance following the recipe in Moster et al. (2011).

The right panel of Figure 9 compares the cluster faint-to-luminous ratio to the field. The light green shaded regions correspond to the 1σ regions of the field faint-to-luminous ratios, taking into account the variation of the evolution correction from different assumptions. From Figure 9 it is evident that clusters have comparable faint-to-luminous ratios as in the field at $z \sim 1.15$. This is consistent with the results of van der Burg et al. (2013), who found that the shape of the stellar mass function of passive galaxies in clusters is comparable to the field at $z \sim 1$. At lower redshifts, the ratio in clusters becomes higher than that of the field. Interestingly, while the faint-to-luminous ratios in clusters evolve strongly with redshift, the ratios in the field show a much milder redshift dependence and is consistent with no evolution. This result is in contrast with

the evolution seen by Gilbank & Balogh (2008). We notice that, however, given the large uncertainties in the data points in Gilbank & Balogh (2008) (see Figure 9), the only difference that is $> 1\sigma$ is their highest redshift bin at $z \sim 0.9$, which comes from first epoch VVDS data (Zucca et al. 2006). We therefore suspect the difference is mainly due to the depth and area coverage of the catalogue.

Figure 9 demonstrates that the environment plays an important role in shaping the build up of the passive population. The mild redshift dependence in the field ratios suggests that newly quenched galaxies are being added in both the bright end and the faint end of the population by a similar fraction. Indeed, the number density of the bright and faint galaxies in the field have both grown by a factor of ~ 4 from the highest redshift bin ($z \sim 1.15$) to the lowest redshift bin ($z \sim 0.15$). Note that the split magnitude between bright and faint galaxies ($M_{V,\mathrm{vega}} = -20$) roughly corresponds to $\log(M_*/M_\odot) \sim 10.2 - 10.5$[6]. The mild redshift dependence in the field ratios is therefore consistent with previous studies on stellar mass function of passive galaxies in the field, which have found significant growth in both the high-mass end and low-mass end from $z \sim 1$ to $z \sim 0$ (e.g. Muzzin et al. 2013b; Tomczak et al. 2014). The growth is commonly attributed to various mass-quenching processes internal to the galaxies, such as energetic feedback from supernovae and stellar winds for low-mass galaxies (e.g. Dekel & Silk 1986; Hopkins et al. 2014) and ejective feedback from active galactic nuclei (AGN) for more massive galaxies (e.g. Bower et al. 2006; Terrazas et al. 2016). Given that the field ratios do not evolve strongly with redshift, it is evident that the strong redshift dependence of the cluster ratios is a result of the high-density environment and that preferentially low (or moderate) mass galaxies are quenched by the environment. Additionally, the difference between the cluster and field ratios suggests that the quenching effects induced by environment are clearer at low redshifts. This

_____

[6] This M/L conversion is derived using a range of SSP models, assuming $z_f = 0.5 - 4.0$ and $Z = Z_\odot$.

is consistent with the mostly mass-independent environmental quenching scenario established at low redshift (e.g. Peng et al. 2010). Since the LF of star-forming galaxies is steeper at the faint end, a population of environmentally quenched galaxies would have a relatively high faint-to-luminous ratio. Recent studies of infalling galaxies in local groups and clusters have demonstrated that the ram pressure stripping of the cold gas in the galaxies when it passes through the ICM is the dominant mechanism (e.g. Boselli et al. 2016; Fillingham et al. 2016; Fossati et al. 2018), although strangulation may also play a significant role (for galaxies with $\log(M_*/M_\odot) < 11$, see e.g. Fillingham et al. 2015; Peng et al. 2015).

Although we will not be able to identify the main quenching mechanism at $z \sim 1.15$ using only the faint-to-luminous ratios, from Figure 9 we can see that the effect of environmental quenching in the ratios only emerges after $z < 1$. The naive interpretation is that environmental quenching is negligible, but this cannot be true as various works have shown that the passive fraction for massive galaxies in clusters are at least 30% higher than the field at this redshift range, suggesting that environmental quenching is at work (i.e. with a non-zero environmental quenching efficiency, Nantais et al. 2016, 2017; Foltz et al. 2018). The next simplest explanation is then that clusters at $z \sim 1.15$ have higher fraction of both bright and faint passive galaxies than the field due to environmental quenching effects, but in a way that the faint-to-luminous ratio has to remain consistent with the field.

The implication of the above explanation is worth exploring, as it provides constraints on the relative fraction of bright and faint galaxies that are environmentally quenched. To further investigate its connection to the environmental quenching mechanism, a robust measurement of the star forming galaxy luminosity function is required. With the full GOGREEN sample, we will be able to study and model in detail the evolution of both passive and star-forming populations in these high-density environments up to $z \sim 1.5$, but it is not possible with this preliminary analysis.

6. SUMMARY AND CONCLUSIONS

In this paper we have presented the rest-frame H-band luminosity function and faint-to-luminous ratio of red sequence galaxies in seven clusters at $1.0 < z < 1.3$ from the Gemini Observations of Galaxies in Rich Early Environments Survey (GOGREEN). We compare the composite red sequence LFs of these clusters with a sample of EDisCS clusters at $z \sim 0.6$ to investigate the build up of the red sequence. Our results can be summarised as follows:

- The red sequence LF of all seven clusters shows a gradual decrease towards the faint end. By stacking the entire sample, we derive a shallow cluster-average faint end slope of $\alpha \sim -0.35^{+0.15}_{-0.15}$ and $M_H^* \sim -23.52^{+0.15}_{-0.17}$ using the MLE approach.

- We compare the composite LF of the GOGREEN clusters to a sample of EDisCS clusters at $z \sim 0.6$. After applying the passive evolution correction and renormalising the composite LF to have the same halo mass as the EDisCS clusters, we find that the bright end of the two LFs are consistent with each other. This suggests that most of the bright passive population in clusters are already assembled at $z \sim 1.15$. The evolution corrected M_H^* of the two LFs are also consistent with each other. On the other hand, the composite

LF of the GOGREEN clusters shows a shallower slope on the faint end compared to the EDisCS clusters (full EDisCS sample: $\alpha \sim -0.90^{+0.13}_{-0.15}$, selected EDisCS sample that are plausible descendants of GOGREEN clusters: $\alpha \sim -0.91^{+0.15}_{-0.17}$), implying that there is a build up of faint red sequence galaxies over time.

- By integrating the red sequence LFs of the passive evolution corrected and renormalised GOGREEN and EDisCS sample, we find that the total red sequence luminosities grow by $\sim 31\% \pm 30\%$ (full EDisCS sample, $\sim 13\% \pm 28\%$ if comparing with the selected EDisCS sample) over the ~ 2.6 Gyrs between $z \sim 1.15$ and $z \sim 0.60$. The growth comes mostly from the faint end ($M_H > -23$, passive evolution corrected), the mean luminosity of the faint end grows by almost a factor of two, while the bright end ($M_H \leq -23$) of the GOGREEN clusters is completely consistent with EDisCS. Note that BCGs are excluded from the red sequence LFs of both samples.

- There is a general trend of decreasing faint-to-luminous ratio with increasing redshift when comparing the ratio of the GOGREEN clusters ($0.78^{+0.19}_{-0.15}$) with literature values at lower redshifts, suggesting that the build-up of the faint red sequence galaxies occurs gradually since $z \sim 1.15$. The amount of decrease is consistent with the evolution predicted in previous studies.

- Comparing the faint-to-luminous ratios of the clusters to those of the field, we find that they show different evolution with redshift. At $z \sim 1.15$, clusters have consistent faint-to-luminous ratios as the field. The ratios of the field only show a mild redshift dependence since $z \sim 1$. We have explored various assumptions in deriving the passive evolution correction for the ratios of the field, therefore our findings are robust to reasonable uncertainties in the evolution corrections. The strong redshift evolution of the cluster ratios demonstrates that the environment plays an important role in shaping the build up of the passive population. The fact that clusters show consistent faint-to-luminous ratios as in the field suggest that both bright and faint cluster galaxies experience the quenching effect induced by environment, and provide constraints on the relative fraction of bright and faint galaxies that are environmentally quenched at high redshift.

REFERENCES

Agulli, I., Aguerri, J. A. L., Sánchez-Janssen, R., et al. 2014, MNRAS, 444, L34

Aihara, H., Arimoto, N., Armstrong, R., et al. 2018, PASJ, 70, S4

Alshino, A., Khosroshahi, H., Ponman, T., et al. 2010, MNRAS, 401, 941

Andreon, S. 2006, MNRAS, 369, 969

—. 2008, MNRAS, 386, 1045

Andreon, S., Newman, A. B., Trinchieri, G., et al. 2014, A&A, 565, A120

Annunziatella, M., Biviano, A., Mercurio, A., et al. 2014, A&A, 571, A80

Annunziatella, M., Mercurio, A., Biviano, A., et al. 2016, A&A, 585, A160

Aragon-Salamanca, A., Ellis, R. S., Couch, W. J., & Carter, D. 1993, MNRAS, 262, 764

Ascaso, B., Lemaux, B. C., Lubin, L. M., et al. 2014, MNRAS, 442, 589

Astropy Collaboration, Robitaille, T. P., Tollerud, E. J., et al. 2013, A&A, 558, A33

Baldry, I. K., Balogh, M. L., Bower, R. G., et al. 2006, MNRAS, 373, 469

Baldry, I. K., Glazebrook, K., Brinkmann, J., et al. 2004, ApJ, 600, 681

Balogh, M. L., Baldry, I. K., Nichol, R., et al. 2004, ApJ, 615, L101

Balogh, M. L., Morris, S. L., Yee, H. K. C., Carlberg, R. G., & Ellingson, E. 1997, ApJ, 488, L75

Balogh, M. L., McGee, S. L., Mok, A., et al. 2016, MNRAS, 456, 4364

Balogh, M. L., Gilbank, D. G., Muzzin, A., et al. 2017, MNRAS, 470, 4168

Barkhouse, W. A., Yee, H. K. C., & López-Cruz, O. 2007, ApJ, 671, 1471

Barrena, R., Girardi, M., Boschin, W., & Mardirossian, F. 2012, A&A, 540, A90

Bell, E. F., McIntosh, D. H., Katz, N., & Weinberg, M. D. 2003, ApJS, 149, 289

Bell, E. F., Wolf, C., Meisenheimer, K., et al. 2004, ApJ, 608, 752

Bellstedt, S., Lidman, C., Muzzin, A., et al. 2016, MNRAS, 460, 2862

Berry, D., Currie, M., Jenness, T., et al. 2013, in Astronomical Society of the Pacific Conference Series, Vol. 475, Astronomical Data Analysis Software and Systems XXII, ed. D. N. Friedel, 247

Bertin, E., & Arnouts, S. 1996, A&AS, 117, 393

Bertin, E., Mellier, Y., Radovich, M., et al. 2002, in Astronomical Society of the Pacific Conference Series, Vol. 281, Astronomical Data Analysis Software and Systems XI, ed. D. A. Bohlender, D. Durand, & T. H. Handley, 228

Bildfell, C., Hoekstra, H., Babul, A., et al. 2012, MNRAS, 425, 204

Biviano, A., Durret, F., Gerbal, D., et al. 1995, A&A, 297, 610

Bleem, L. E., Stalder, B., de Haan, T., et al. 2015, ApJS, 216, 27

Bond, J. R., Cole, S., Efstathiou, G., & Kaiser, N. 1991, ApJ, 379, 440

Bosch, J., Armstrong, R., Bickerton, S., et al. 2018, PASJ, 70, S5

Boselli, A., & Gavazzi, G. 2006, PASP, 118, 517

—. 2014, A&A Rev., 22, 74

Boselli, A., Cuillandre, J. C., Fossati, M., et al. 2016, A&A, 587, A68

Bower, R. G., Benson, A. J., Malbon, R., et al. 2006, MNRAS, 370, 645

Bower, R. G., Kodama, T., & Terlevich, A. 1998, MNRAS, 299, 1193

Bower, R. G., Lucey, J. R., & Ellis, R. S. 1992, MNRAS, 254, 589

Brammer, G. B., van Dokkum, P. G., & Coppi, P. 2008, ApJ, 686, 1503

Brodwin, M., Ruel, J., Ade, P. A. R., et al. 2010, ApJ, 721, 90

Bruzual, G., & Charlot, S. 2003, MNRAS, 344, 1000

Bulbul, E., Chiu, I.-N., Mohr, J. J., et al. 2019, ApJ, 871, 50

Capozzi, D., Collins, C. A., & Stott, J. P. 2010, MNRAS, 403, 1274

Cattaneo, A., Dekel, A., Faber, S. M., & Guiderdoni, B. 2008, MNRAS, 389, 567

Cerulo, P., Couch, W. J., Lidman, C., et al. 2016, MNRAS, 457, 2209

Chabrier, G. 2003, PASP, 115, 763

Colless, M. 1989, MNRAS, 237, 799

Contini, E., De Lucia, G., Villalobos, Á., & Borgani, S. 2014, MNRAS, 437, 3787

Contini, E., Yi, S. K., & Kang, X. 2018, MNRAS, 479, 932

Cooper, M. C., Gallazzi, A., Newman, J. A., & Yan, R. 2010, MNRAS, 402, 1942

Correa, C. A., Wyithe, J. S. B., Schaye, J., & Duffy, A. R. 2015a, MNRAS, 450, 1514

—. 2015b, MNRAS, 450, 1521

—. 2015c, MNRAS, 452, 1217

Cowie, L. L., Songaila, A., Hu, E. M., & Cohen, J. G. 1996, AJ, 112, 839

Crawford, S. M., Bershady, M. A., & Hoessel, J. G. 2009, ApJ, 690, 1158

De Lucia, G., Poggianti, B. M., Aragón-Salamanca, A., et al. 2004, ApJ, 610, L77

—. 2007, MNRAS, 374, 809

De Propris, R., Bremer, M. N., & Phillipps, S. 2015, MNRAS, 450, 1268

De Propris, R., Phillipps, S., & Bremer, M. N. 2013, MNRAS, 434, 3469

De Propris, R., Stanford, S. A., Eisenhardt, P. R., Dickinson, M., & Elston, R. 1999, AJ, 118, 719

De Propris, R., Stanford, S. A., Eisenhardt, P. R., Holden, B. P., & Rosati, P. 2007, AJ, 133, 2209

Dekel, A., & Birnboim, Y. 2006, MNRAS, 368, 2

Dekel, A., & Silk, J. 1986, ApJ, 303, 39

DeMaio, T., Gonzalez, A. H., Zabludoff, A., Zaritsky, D., & Bradač, M. 2015, MNRAS, 448, 1162

DeMaio, T., Gonzalez, A. H., Zabludoff, A., et al. 2018, MNRAS, 474, 3009

Demarco, R., Wilson, G., Muzzin, A., et al. 2010a, ApJ, 711, 1185

Demarco, R., Gobat, R., Rosati, P., et al. 2010b, ApJ, 725, 1252

Dressler, A. 1980, ApJ, 236, 351

Dressler, A., Oemler, Jr., A., Couch, W. J., et al. 1997, ApJ, 490, 577

Driver, S. P., Allen, P. D., Graham, A. W., et al. 2006, MNRAS, 368, 414

Ebeling, H. 2003, MNRAS, 340, 1269

Ellis, R. S., Smail, I., Dressler, A., et al. 1997, ApJ, 483, 582

Evrard, A. E., Bialek, J., Busha, M., et al. 2008, ApJ, 672, 122

Fillingham, S. P., Cooper, M. C., Pace, A. B., et al. 2016, MNRAS, 463, 1916

Fillingham, S. P., Cooper, M. C., Wheeler, C., et al. 2015, MNRAS, 454, 2039

Foley, R. J., Andersson, K., Bazin, G., et al. 2011, ApJ, 731, 86

Foltz, R., Wilson, G., Muzzin, A., et al. 2018, ArXiv e-prints, arXiv:1803.03305

Fossati, M., Mendel, J. T., Boselli, A., et al. 2018, A&A, 614, A57

Fumagalli, M., Fossati, M., Hau, G. K. T., et al. 2014, MNRAS, 445, 4335

Gilbank, D. G., & Balogh, M. L. 2008, MNRAS, 385, L116

Gilbank, D. G., Yee, H. K. C., Ellingson, E., et al. 2008, ApJ, 673, 742

Gonzalez, A. H., Zaritsky, D., Dalcanton, J. J., & Nelson, A. 2001, ApJS, 137, 117

Gunn, J. E., & Gott, III, J. R. 1972, ApJ, 176, 1

Gupta, N., Saro, A., Mohr, J. J., Dolag, K., & Liu, J. 2017, MNRAS, 469, 3069

Halliday, C., Milvang-Jensen, B., Poirier, S., et al. 2004, A&A, 427, 397

Hopkins, P. F., Bundy, K., Hernquist, L., & Ellis, R. S. 2007, ApJ, 659, 976

Hopkins, P. F., Kereš, D., Oñorbe, J., et al. 2014, MNRAS, 445, 581

Kawinwanichakij, L., Papovich, C., Quadri, R. F., et al. 2017, ApJ, 847, 134

Kodama, T., & Arimoto, N. 1997, A&A, 320, 41

Kodama, T., Arimoto, N., Barger, A. J., & Arag'on-Salamanca, A. 1998, A&A, 334, 99

Kodama, T., Yamada, T., Akiyama, M., et al. 2004, MNRAS, 350, 1005

Kriek, M., van Dokkum, P. G., Labbé, I., et al. 2009, ApJ, 700, 221

Kron, R. G. 1980, ApJS, 43, 305

Labbé, I., Franx, M., Rudnick, G., et al. 2003, AJ, 125, 1107

Labbé, I., Huang, J., Franx, M., et al. 2005, ApJ, 624, L81

Lacey, C., & Cole, S. 1993, MNRAS, 262, 627

Lan, T.-W., Ménard, B., & Mo, H. 2016, MNRAS, 459, 3998
Larson, R. B., Tinsley, B. M., & Caldwell, C. N. 1980, ApJ, 237, 692
Lidman, C., Suherli, J., Muzzin, A., et al. 2012, MNRAS, 427, 550
Lin, Y.-T., Brodwin, M., Gonzalez, A. H., et al. 2013, ApJ, 771, 61
Lin, Y.-T., Mohr, J. J., Gonzalez, A. H., & Stanford, S. A. 2006, ApJ, 650, L99
Mamon, G. A., Biviano, A., & Boué, G. 2013, MNRAS, 429, 3079
Mancone, C. L., & Gonzalez, A. H. 2012, PASP, 124, 606
Mancone, C. L., Baker, T., Gonzalez, A. H., et al. 2012, ApJ, 761, 141
Maraston, C. 2005, MNRAS, 362, 799
Marchesini, D., van Dokkum, P., Quadri, R., et al. 2007, ApJ, 656, 42
Martel, H., Barai, P., & Brito, W. 2012, ApJ, 757, 48
Martinet, N., Durret, F., Adami, C., & Rudnick, G. 2017, A&A, 604, A80
Martinet, N., Durret, F., Guennou, L., et al. 2015, A&A, 575, A116
Martis, N. S., Marchesini, D., Brammer, G. B., et al. 2016, ApJ, 827, L25
Mauduit, J.-C., Lacy, M., Farrah, D., et al. 2012, PASP, 124, 714
McGee, S. L., Bower, R. G., & Balogh, M. L. 2014, MNRAS, 442, L105
Milvang-Jensen, B., Noll, S., Halliday, C., et al. 2008, A&A, 482, 419
Moore, B., Lake, G., & Katz, N. 1998, ApJ, 495, 139
Moretti, A., Bettoni, D., Poggianti, B. M., et al. 2015, A&A, 581, A11
Moster, B. P., Somerville, R. S., Newman, J. A., & Rix, H.-W. 2011, ApJ, 731, 113
Muzzin, A., Marchesini, D., van Dokkum, P. G., et al. 2009, ApJ, 701, 1839
Muzzin, A., Wilson, G., Lacy, M., Yee, H. K. C., & Stanford, S. A. 2008, ApJ, 686, 966
Muzzin, A., Yee, H. K. C., Hall, P. B., Ellingson, E., & Lin, H. 2007, ApJ, 659, 1106
Muzzin, A., Wilson, G., Yee, H. K. C., et al. 2012, ApJ, 746, 188
Muzzin, A., Marchesini, D., Stefanon, M., et al. 2013a, ApJS, 206, 8
—. 2013b, ApJ, 777, 18
Nantais, J. B., van der Burg, R. F. J., Lidman, C., et al. 2016, A&A, 592, A161
Nantais, J. B., Muzzin, A., van der Burg, R. F. J., et al. 2017, MNRAS, 465, L104
Nelan, J. E., Smith, R. J., Hudson, M. J., et al. 2005, ApJ, 632, 137
Oke, J. B., & Gunn, J. E. 1983, ApJ, 266, 713
Papovich, C., Kawinwanichakij, L., Quadri, R. F., et al. 2018, ApJ, 854, 30
Pelló, R., Rudnick, G., De Lucia, G., et al. 2009, A&A, 508, 1173
Peng, Y., Maiolino, R., & Cochrane, R. 2015, Nature, 521, 192
Peng, Y.-j., Lilly, S. J., Kovač, K., et al. 2010, ApJ, 721, 193
Pimbblet, K. A., Smail, I., Kodama, T., et al. 2002, MNRAS, 331, 333
Popesso, P., Biviano, A., Böhringer, H., & Romaniello, M. 2006, A&A, 445, 29
Popesso, P., Böhringer, H., Romaniello, M., & Voges, W. 2005, A&A, 433, 415
Rasia, E., Meneghetti, M., Martino, R., et al. 2012, New Journal of Physics, 14, 055018
Rudnick, G., von der Linden, A., Pelló, R., et al. 2009, ApJ, 700, 1559
Rudnick, G. H., Tran, K.-V., Papovich, C., Momcheva, I., & Willmer, C. 2012, ApJ, 755, 14

Ruel, J., Bazin, G., Bayliss, M., et al. 2014, ApJ, 792, 45
Sánchez-Blázquez, P., Jablonka, P., Noll, S., et al. 2009, A&A, 499, 47
Sandage, A., Tammann, G. A., & Yahil, A. 1979, ApJ, 232, 352
Sandage, A., & Visvanathan, N. 1978, ApJ, 225, 742
Sanders, D. B., Salvato, M., Aussel, H., et al. 2007, ApJS, 172, 86
Saro, A., Mohr, J. J., Bazin, G., & Dolag, K. 2013, ApJ, 772, 47
Sarron, F., Martinet, N., Durret, F., & Adami, C. 2018, A&A, 613, A67
Scarlata, C., Carollo, C. M., Lilly, S. J., et al. 2007, ApJS, 172, 494
Schechter, P. 1976, ApJ, 203, 297
Schlafly, E. F., & Finkbeiner, D. P. 2011, ApJ, 737, 103
Schlegel, D. J., Finkbeiner, D. P., & Davis, M. 1998, ApJ, 500, 525
Sersic, J. L. 1968, Atlas de galaxias australes
Smail, I., Edge, A. C., Ellis, R. S., & Blandford, R. D. 1998, MNRAS, 293, 124
Smith, R. J. 2005, MNRAS, 359, 975
Smith, R. J., Lucey, J. R., Price, J., Hudson, M. J., & Phillipps, S. 2012, MNRAS, 419, 3167
Spitler, L. R., Straatman, C. M. S., Labbé, I., et al. 2014, ApJ, 787, L36
Stalder, B., Ruel, J., Šuhada, R., et al. 2013, ApJ, 763, 93
Stanford, S. A., Eisenhardt, P. R., & Dickinson, M. 1998, ApJ, 492, 461
Stott, J. P., Pimbblet, K. A., Edge, A. C., Smith, G. P., & Wardlow, J. L. 2009, MNRAS, 394, 2098
Stott, J. P., Smail, I., Edge, A. C., et al. 2007, ApJ, 661, 95
Strazzullo, V., Rosati, P., Pannella, M., et al. 2010, A&A, 524, A17
Tanaka, M., Kodama, T., Arimoto, N., et al. 2005, MNRAS, 362, 268
Tanaka, M., Kodama, T., Kajisawa, M., et al. 2007, MNRAS, 377, 1206
Tanaka, M., Hasinger, G., Silverman, J. D., et al. 2017, ArXiv e-prints, arXiv:1706.00566
Terrazas, B. A., Bell, E. F., Henriques, B. M. B., et al. 2016, ApJ, 830, L12
Thomas, D., Maraston, C., Bender, R., & Mendes de Oliveira, C. 2005, ApJ, 621, 673
Thomas, D., Maraston, C., Schawinski, K., Sarzi, M., & Silk, J. 2010, MNRAS, 404, 1775
Tomczak, A. R., Quadri, R. F., Tran, K.-V. H., et al. 2014, ApJ, 783, 85
Trager, S. C., Faber, S. M., & Dressler, A. 2008, MNRAS, 386, 715
van den Bosch, F. C., Jiang, F., Hearin, A., et al. 2014, MNRAS, 445, 1713
van der Burg, R. F. J., Hoekstra, H., Muzzin, A., et al. 2015, A&A, 577, A19
van der Burg, R. F. J., Muzzin, A., Hoekstra, H., et al. 2013, A&A, 557, A15
van der Wel, A., Franx, M., van Dokkum, P. G., et al. 2014, ApJ, 788, 28
Wetzel, A. R., Tinker, J. L., & Conroy, C. 2012, MNRAS, 424, 232
White, S. D. M., Clowe, D. I., Simard, L., et al. 2005, A&A, 444, 365
Williams, R. J., Quadri, R. F., Franx, M., van Dokkum, P., & Labbé, I. 2009, ApJ, 691, 1879
Wilson, G., Muzzin, A., Yee, H. K. C., et al. 2009, ApJ, 698, 1943
Wolf, C., Gray, M. E., & Meisenheimer, K. 2005, A&A, 443, 435
Woo, J., Dekel, A., Faber, S. M., et al. 2013, MNRAS, 428, 3306
Zenteno, A., Mohr, J. J., Desai, S., et al. 2016, MNRAS, 462, 830
Zhang, Y., Miller, C. J., Rooney, P., et al. 2017, ArXiv e-prints, arXiv:1710.05908
Zucca, E., Ilbert, O., Bardelli, S., et al. 2006, A&A, 455, 879

APPENDIX

MATCHING OF FILTER PASSBANDS FOR STATISTICAL BACKGROUND SUBTRACTION

As we mentioned in Section 3.1, in the ideal case of statistical field subtraction the field catalogue should have the same depth and passband as the cluster photometry. Although this is often not the case in reality, occasionally one can utilise the additional passbands available in the control field catalogue to achieve a nearly perfect match. In this section we expand on the discussion in Section 3.1.1 on how we use both the z and y-band data of HSC-SSP to match the passband of the GMOS z'-band.

Figure 10 shows the transmission curve of the Gemini/GMOS z' filters and Subaru/HSC z and y filters used in this work. The wavelength coverage of the GMOS-S and GMOS-N z' filters are much wider and extend further to the red compared to the HSC z filters. In fact, the GMOS z' filters cover further to the red wavelength compared to most z-band filters, due to the outstanding red-sensitivities of the e2v DD and Hamamatsu detectors on Gemini North and South (blue and orange dotted curve). It can be seen that the GMOS z' band almost covers both HSC z and y-bands.

The next step is to derive the color term between the GMOS z' and HSC filters. We test the stability of the color terms with redshift by computing apparent magnitudes of BC03 SSP models with a range of formation redshifts and metallicities in different filters. The result of GMOS-S is shown in Figure 11 as an example. The optimal color term between two filters for statistical field subtraction should be flat at all redshifts, so that one does not under- or over-subtract galaxy populations at a certain redshift range and bias the resulting LF. Nevertheless, due to the difference in the wavelength coverage between the GMOS and HSC filters, one can see from the top and middle panels of Figure 11 that there are various troughs and peaks at different redshifts, due to spectral features being redshifted into the filter coverage. Hence, we use a combination of HSC z and y-band magnitudes to match the passband of the GMOS z' filters, shown in the bottom panel. It is clear that the stability of the color term with redshift is vastly
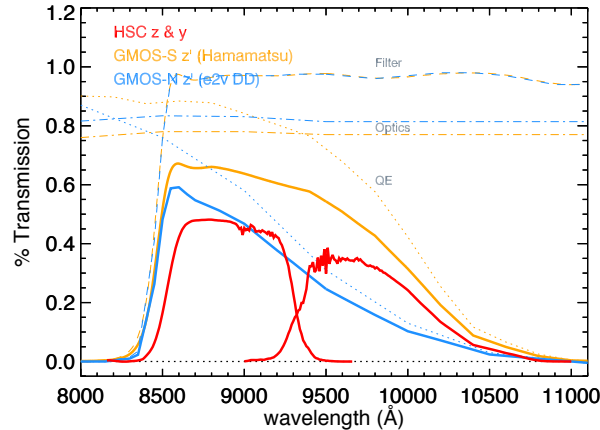
Fig. 10.— The wavelength response of the Gemini/GMOS z' filters and the Subaru/HSC z and y filters. Orange lines show the total wavelength response (solid) of the GMOS-S z' filter (dashed), the Gemini South telescope response (dot-dashed) and the QE of the Hamamatsu detector (dotted). Similarly, blue lines correspond to the GMOS-N z' filter (dashed), the Gemini North telescope response (dot-dashed) and the QE of the e2V DD detector (dotted). Red lines correspond to the HSC total response with z and y filters. It can be seen that the GMOS z'-band has a much longer effective wavelength compared to the HSC z-band. Hence, a combination of the HSC z and y filters is used to match the GMOS z' filters for statistical background subtraction.

improved when a combination of the two bands is used. The variation (~ 0.02 mag) is smaller than the photometric uncertainty of most objects we are interested in. The color term used for GMOS-S is ~ 0.02 mag, while the one used for GMOS-N is ~ 0.01 mag. We note that using other SSP models (e.g. Maraston 2005) gives similar results as these are broad-band colors. These color terms are then applied while comparing the color-magnitude diagram of the cluster and the field to obtain cluster membership probabilities for individual galaxies.

DOES THE LF DEPEND ON HALO MASS?

One interesting question regarding cluster LFs concerns the possible dependence of the red sequence LF on cluster mass. Previous studies at intermediate redshifts ($0.5 < z < 0.8$) have shown, by examining faint-to-luminous ratio or α of the LF, that high mass clusters may evolve at a faster rate than low mass ones at similar redshifts (e.g. Tanaka et al. 2005; De Lucia et al. 2007; Gilbank et al. 2008; Martinet et al. 2015). In this section we examine this dependence with our sample at $z \sim 1$.

We split our sample into two bins in halo mass (see Table 1) and derive a composite LF for each bin. The low mass bin comprises five clusters with $13.9 \leq \log(M_{200}/M_{\odot}) \leq 14.6$, while the high mass bin comprises the remaining two massive clusters with $14.8 \leq \log(M_{200}/M_{\odot}) \leq 14.9$. We find that α and M_H^* of the two composite LFs are consistent with each other. Using a radius limit of $R \leq 0.5R_{200}$ instead of $R \leq 0.75$ Mpc also gives a similar result. The best fitting α and M_H^* can be found in Table 3. Similarly, the faint-to-luminous ratios show no obvious trend with halo mass in our sample.

However, it is entirely possible that the dependence is hindered by the small number of clusters here and the large uncertainties in the derived quantities. Gilbank et al. (2008) measured a $\sim 2\sigma$ difference in the faint-to-luminous ratios (luminous-to-faint ratio in their work) between poor and rich clusters at $z \sim 0.9$ with 98 clusters. Therefore it is very likely that with a factor of 10 smaller sample we are not able to see such a small difference. With the full GOGREEN sample which triples the number of clusters used here, we might be able to discern and constrain the possible dependence with halo mass.

IS THERE ANY RADIAL DEPENDENCE?

A number of works on local to intermediate redshift clusters have reported that the shape of the LF varies with radius, they found that the faint end slope α becomes less positive (i.e. steeper) with increasing selection radius (e.g. Popesso et al. 2006; Barkhouse et al. 2007; Crawford et al. 2009). Other works, however, find little or no evidence of radial dependence (e.g. Barrena et al. 2012; Martinet et al. 2015, 2017), or that the difference can only be seen in the densest region of the cluster ($R < 0.25R_{200}$, Annunziatella et al. 2014, 2016).

Here we investigate the radial dependence of the LF in our sample. Due to the small number of clusters we have, we split the LF that is derived with a selection radius of $R \leq 1.0$ Mpc into two radial sections: $R \leq 0.5$ Mpc (inner) and $0.5 < R \leq 1.0$ Mpc (outer). The result is shown in Figure 12. We found that the outer radial section shows a steeper slope with $\alpha = -0.57^{+0.22}_{-0.26}$ than the inner one ($\alpha = -0.17^{+0.19}_{-0.20}$), although the difference is only $\sim 1\sigma$ given the large uncertainties in the derived α. Comparing the number counts, the $R \leq 1.0$ Mpc LF is mostly dominated by the inner section. Unfortunately we cannot test if this difference is due to the cluster core as suggested by Annunziatella et al. (2014, 2016), as there is not enough number statistics to accurately determine Schechter parameters if we adopt a selection radius of $R < 0.25R_{200}$. Similar to the halo-mass dependence, we will be able to better constrain this radial dependence with the full GOGREEN sample.
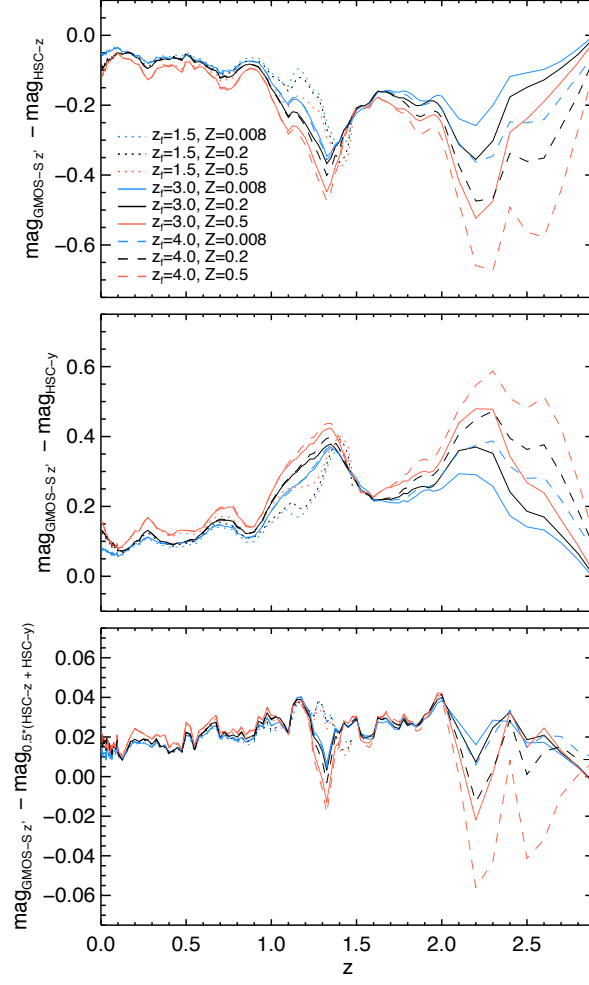
FIG. 11.— The color term between the GMOS-S z' and HSC filters with redshift. Top to bottom: Difference in apparent magnitudes of SSP models between GMOS z' and HSC z, GMOS z' and HSC y, and GMOS z' and a combination of HSC z and y as a function redshift. Blue, black and red curves correspond to models with a metallicity of $Z = 0.4Z_\odot$, $Z_\odot$, $2.5Z_\odot$, while the solid, dotted and dashed line styles correspond to models with formation redshift of $z_f = 1.5, 3.0, 4.0$, respectively.
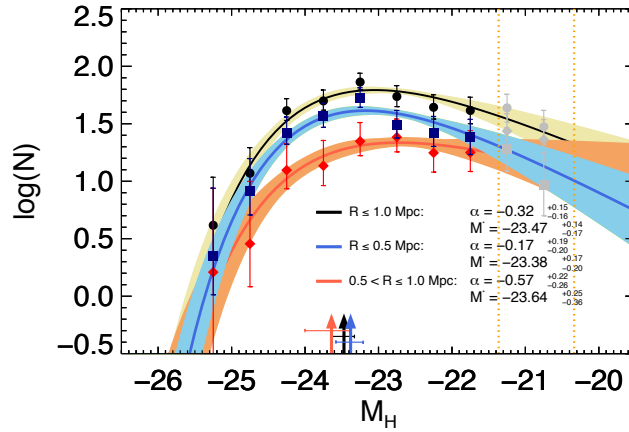

FIG. 12.— Cluster-centric radial dependence of the rest-frame H-band red sequence LF of the seven GOGREEN clusters. Same as Figure 3, but for $R \le 1.0$ Mpc. The blue and red lines correspond to the best-fitting Schechter functions to the inner and outer LFs with a selected radial range of $R \le 0.5$ Mpc and $0.5 < R \le 1.0$ Mpc, respectively.

POTENTIAL EFFECT OF SOURCE BLENDING ON THE LF

In this work we use PSF-matched $2''$ diameter $z' - [3.6]$ color measurements and pseudo-total 3.6 μm magnitudes to construct the GOGREEN LF (see Section 2.2 for details). A common concern with IRAC photometry is source blending issues due to its large-FWHM PSF. Source blending can result in inaccurate photometry (i.e. flux contamination from neighbouring objects) or the failure to detect a galaxy entirely (i.e. missing detections). In the case of our analysis, missing galaxies because of blending is not a concern as we used unconvolved z'-band images instead of the 3.6 μm images as the detection band. Inaccurate photometry due to source blending, on the other hand, can be a source of uncertainty or bias to our LF. Here we give an estimate of how flux contamination from neighbors would affect our results.

Inaccurate photometry from source blending mainly affects the selection of red sequence galaxies in color-magnitude space. One thing to note is that the effect of source blending can go in two ways: 1) objects that should lie outside the red sequence selection region can scatter into the red sequence, thus increasing the apparent number of red sequence galaxies. 2) Objects in the red sequence can also drop out of our red sequence selection due to flux contamination from their neighbours, and thus decreasing the apparent number of red sequence galaxies. Since the effect of blending is usually more severe for faint objects, the former would result in a LF that is steeper (i.e. α being less positive) and the latter would result in a LF with an apparent α that is more positive. In this section we focus on the latter as its effect is more relevant to our findings.

The first step is to determine the conditions under which the photometry of the object of interest is contaminated by its neighbor. To do this we have constructed a simulation by putting sets of objects and 'neighbors' as functions of separation distance, 3.6 μm object magnitude and neighbour magnitude on the images. All sources are set to a size of ~ 1.7 kpc, the median size of a passive galaxy with $\log(M/M_\odot) \sim 10.7$ at $z \sim 1.15$ (van der Wel et al. 2014), and are convolved with the 3.6 μm PSF. By measuring the $2''$ diameter aperture magnitudes, we then define a region on the separation distances-object magnitudes-neighbor magnitudes plane where the resultant colors deviate more than 0.125 mag from the true value as 'contaminated'. This choice of 0.125 mag will be explained below. Objects that are within the region are considered to be severely affected by blending. Using these regions as criteria we then pick out objects in our cluster photometric catalogues that have potentially problematic color due to source blending. A relation of the percentage of these contaminated objects as a function of magnitude is derived. We find that the percentage of these objects increases with 3.6 μm magnitudes; for the GOGREEN clusters on average only $\sim 5\%$ of objects have potentially problematic color at $[3.6] = 18$, while at $[3.6] = 23 \sim 25\%$ of objects may be contaminated according to the criteria.

The next step is to investigate how these objects may impact our results. In addition to the red sequence LF, we construct a stacked LF for the GOGREEN clusters using regions that are right above or below the red sequence (i.e. the two strips on the CMD that are above and below the red sequence selection region), following the same procedure described in Section 3. The width of these two regions are chosen to be 0.25 mag to contain the majority of objects that can drop out of the red sequence due to source blending. Although it may seem arbitrary to use such width, we stress that increasing the width does not change the conclusion of this section as it is (increasingly) less likely to have objects with larger magnitude deviation from source blending. The abovementioned criteria to select 'contaminated' sources is therefore chosen to be half of the width of these regions (i.e. 0.125 mag) as we can assume that this is the average magnitude deviation the objects require to have to drop out of our red sequence selection.

We then combine the LF of these regions with the relation of the percentage of the contaminated objects as a function of magnitude to estimate the number of objects that drop out of the red sequence because of blending. The blue dotted line in Figure 13 shows the result. As expected, there are more of these sources at the faint end compared to the bright end. Even with the addition of these objects to our red sequence LF, we find that the resulting LFs (black and gray dotted lines) are still within 1σ uncertainties of our red sequence LF. Therefore source blending is unlikely to affect our conclusions. We also stress that the blue dotted line is a conservative estimate, as it only concerns sources that drop out of red sequence due to source blending. As we mentioned above in reality there are also sources that scatter into the red sequence as well which affects the LF in the opposite way, thus the overall effect of source blending is even smaller.
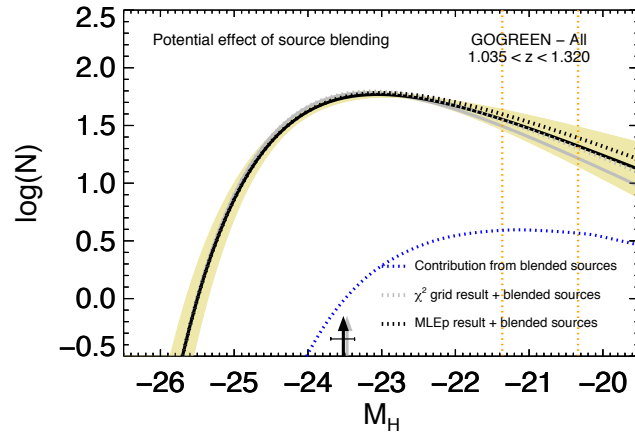
FIG. 13.— Potential effect of source blending to the red sequence LF of the seven GOGREEN clusters. The solid black and grey lines, as well as the vertical arrows correspond to the same LF fits as Figure 3. The blue dotted line correspond to the potential contribution from blended sources that drop out of the red sequence and thus are not accounted for in the LF. The black and grey dotted lines are the sum of the LF fits with this contribution from blended sources. It can be seen that the resultant LFs are still within the 1σ uncertainties of the LF estimated from the MLE method, therefore source blending is unlikely to affect our conclusions.